J. Fluid Mech. (2011), *vol.* 677, *pp.* 103–133. © Cambridge University Press 2011
doi:10.1017/jfm.2011.64

A turbulent patch arising from a breaking internal wave

SERGEY N. YAKOVENKO[1,2], T. GLYN THOMAS[2] AND IAN P. CASTRO[2]†

[1]Institute of Theoretical and Applied Mechanics, Siberian Branch, Russian Academy of Sciences, Novosibirsk 630090, Russia

[2]School of Engineering Sciences, University of Southampton, Highfield, Southampton SO17 1BJ, UK

(Received 13 May 2010; revised 26 January 2011; accepted 3 February 2011; first published online 7 April 2011)

Results of direct numerical simulations of the development of a breaking internal gravity wave are presented. The wave was forced by the imposition of an appropriate bottom boundary shape (a two-dimensional cosine hill) within a density-stratified domain having a uniform upstream velocity and density gradient. The focus is on turbulence generation and maintenance within the turbulent patch generated by the wave breaking. Pathlines, density contours, temporal and spatial spectra, and second moments of the velocity and density fluctuations and turbulent kinetic energy balance terms obtained from the data averaged over the span in the mixed zone are all used in the analysis of the flow. Typical Reynolds numbers, based on the vertical scale of the breaking region and the upstream velocity, were around 6000 and the fully resolved computations yielded sufficient resolution to capture the fine-scale transition processes as well as the subsequent fully developed turbulence. It is shown that globally, within the turbulent patch, there is an approximate balance in the production, dissipation and transport processes for turbulent kinetic energy, so that the patch remains quasi-steady over a significant time. Although it is far from being axially homogeneous, with turbulence generation occurring largely near the upstream bottom part of the patch where the mean velocity shear is particularly large, it has features not dissimilar to those of a classical turbulent wake.

Key words: atmospheric flows, internal waves, turbulence simulation

1. Introduction

Internal gravity waves have an important role in the circulation of atmosphere and oceans, providing mixing and transport of energy and momentum, pollutants and sea animals in both vertical and horizontal directions. Turbulent patches can arise when large-scale internal waves become steep, overturn and break. Such breaking leads to shear (or other) instabilities and then to turbulence which develops into a fully mixed region at the location of the initial wave-breaking. It is a complex phenomenon and often occurs in association with topographically generated lee waves; the resulting effects on aviation safety and local climate have been widely noted (e.g. Clark *et al.*

† Email address for correspondence: i.castro@soton.ac.uk

https://doi.org/10.1017/jfm.2011.64 Published online by Cambridge University Press

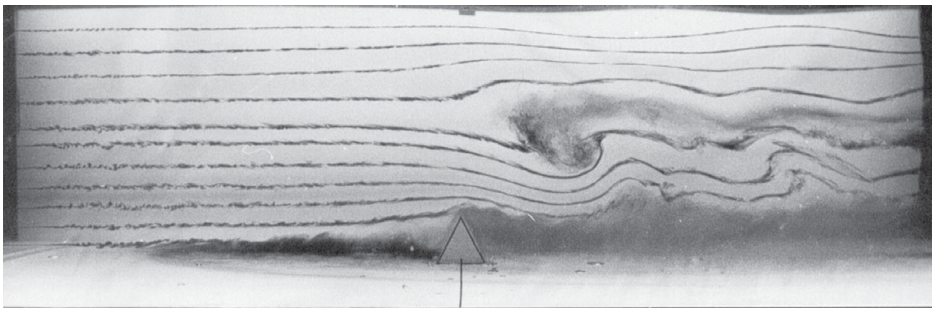


FIGURE 1. A towing tank simulation of the stratified flow (from left to right) over a triangular-shaped obstacle, with $F_h = 0.6$. Pathlines are visualised using dye tracers emitted from an upstream rake.

2000; Grubisic & Lewis 2004, and references therein). There are a number of possible sources of such turbulent patches associated with wave motions (whether in the atmosphere or the oceans). One is a direct result of boundary-layer separation in the lee of the topography, arising from a sufficiently adverse surface pressure gradient enhanced by an elevated lee-wave train. This is *not* convective overturning – i.e. it does not arise because of heavier fluid overlying lighter fluid – but it gives rise nonetheless to a downwind rotor, which becomes turbulent usually through a classical Kelvin–Helmholz (K-H) breakdown within the strong shear layer emanating from the separation point and thus lying above the reversed flow region (see Doyle *et al.* 2005 for a recent exposition of this via large-eddy simulations (LES) of flows over the Rockies).

A second source of turbulent patch arises at much higher elevations from convective overturning of a high-amplitude wave well above the topography. This can happen for uniformly stratified fluid or for situations where there are elevated inversions and/or multiple critical layers between more uniformly stratified layers. Recent examples include Doyle & Durran (2007), in the context of lee waves, and Sveen *et al.* (2002) in the case of a solitary interfacial wave above topography. To fix ideas and as examples of the kind of situation which is addressed in this paper, figures 1 and 2 show, respectively, an experimental and numerical realisation of lee-wave breaking above topography. The first was obtained in a towing tank (obtained during the experiments of Castro & Snyder 1993, but not reported at the time); the triangular body was very wide in the spanwise direction (10 times its height h) and the upstream density gradient, and thus Brunt–Väisälä frequency $N = [-(g/\rho)(\mathrm{d}\rho/\mathrm{d}z)]^{1/2}$, was uniform which, with a fixed towing speed U, yielded a Froude number $F_h = U/Nh$ of 0.6. Note that there are fully turbulent regions nearer the surface (i.e. $z = 0$, with z measured from the bottom of the obstacle) both upstream and downstream of the obstacle, but these are quite separate from the breaking region aloft. Likewise, in the computations of Afanasyev & Peltier (1998), who used a numerical model essentially the same as that first employed for the analysis of topographically forced waves by Clarke & Peltier (1977), the upstream stratification was linear, the obstacle was bell-shaped (and two-dimensional) and $F_h = 1.0$ (figure 2). Potential temperature contours are shown at increasing times after breaking; the turbulent region aloft, separated from the flow nearer the surface, is evident. Note that F_h essentially measures the degree of nonlinearity arising from the bottom boundary condition and it is low values of this parameter which provoke the gravity wave steepening and eventual breaking.

https://doi.org/10.1017/jfm.2011.64 Published online by Cambridge University Press

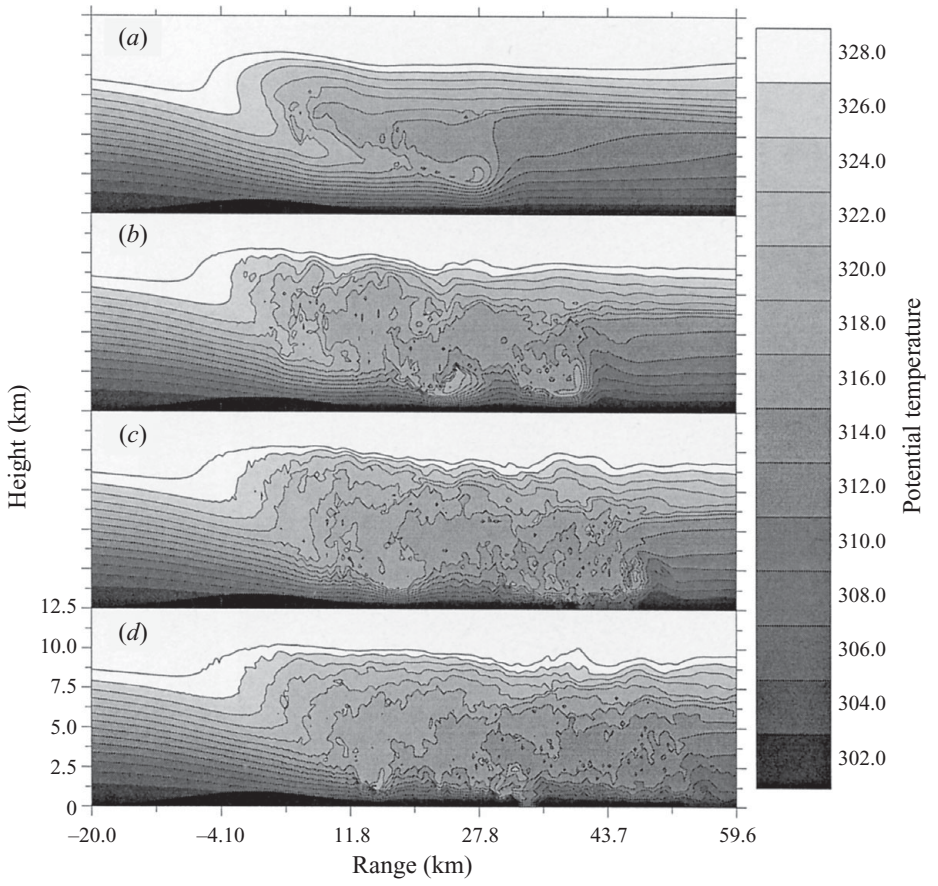


FIGURE 2. Numerical simulation of the stratified flow over a bell-shaped hill (centred at range = 0 km on abscissa axis and extending to about ± 12 km), with $F_h = 1$. (*a–d*) Time increasing from top to bottom. From Afanasyev & Peltier (1998), with permission.

The general problem of lee waves arising in stratified fluids is a classical one and much of the basic literature is covered in Baines (1995). One of the early studies was that of Lilley & Klemp (1979), who solved the classical Long model (Long 1955) for cases of linearly stratified, uniform flow over hills of various shapes, showing how the wave amplitudes depend critically on the nonlinear bottom boundary condition imposed by hills of large amplitude. There have been many laboratory and numerical experiments which confirm the general features delineated by analytical models, at least up to the point of wave-breaking, as discussed by Baines (1995), and a number of these have confirmed that the critical Froude number required for wave-breaking is strongly dependent on, amongst other things, obstacle shape and spanwise aspect ratio. So, for example, for $F_h = 1.0$ an experiment like that illustrated in figure 1 did *not* give breaking waves, unlike the situation in figure 2. Values of F_h much higher than unity are usually too large to yield wave slopes approaching the vertical. The Froude number based on obstacle (axial) length provides a measure of the degree to which the flow is non-hydrostatic. In the present work it is always much lower than F_h, so the full non-hydrostatic equations have been used (although it is worth mentioning that hydrostatic models can be useful even in flows containing wave-breaking, e.g. Smith 1985).

https://doi.org/10.1017/jfm.2011.64 Published online by Cambridge University Press

What is much less clear, however, is the detailed characteristics of the turbulent patch that arises subsequent to wave-breaking, when the classical theories generally break down and cannot properly describe the motion even outside the patch, given the uncertain behaviour of the latter. Probing the turbulent patch by laboratory experiment is very difficult, but numerical studies are beginning to make some progress. Gheusi, Stein & Eiff (2000), for example, used direct numerical simulation (DNS), albeit at very low Reynolds numbers, to explore the wave-breaking flows found in associated experiments (Eiff & Bonneton 2000) and, in the field, there are some LES of specific atmospheric events, which have sought to explore the post-breaking turbulence behaviour (e.g. Doyle *et al.* 2005 noted above). Likewise, there are a number of similar explorations in the oceanographic context (e.g. Smyth, Moum & Caldwell 2001). However, such works are generally either at too low a Reynolds number to be sure that the turbulence patch behaves as it would in practical situations, or require subgrid treatments and relatively large-scale meshes, with the associated modelling uncertainties.

Specific issues addressed in the present paper include questions concerning the longer-term source and maintenance of the turbulence, given that the patch can be long-lived compared with typical turbulence time scales within it, whether a classical (neutral flow) inertial subrange exists, where the major dissipative regions are, whether turbulent transport is a significant component of the turbulent kinetic energy (TKE) balance within the patch, and where (and if) in the patch buoyant production is significant. Our work in one sense follows the example of Gheusi *et al.* (2000), by using DNS to explore the dynamics of a turbulent patch generated by a breaking wave in the lee of topography, for one of the classically simple scenarios – linearly stratified flow over a surface-mounted obstacle. No other complicating factors such as rotational effects, often included in computations of practical atmospheric cases, are considered. However, the Reynolds numbers are at least an order of magnitude higher than previously attempted – similar in fact to those used in the much larger-scale towing tank experiments of Castro, Snyder & Marsh (1983), Castro & Snyder (1993) and, more recently, Eiff, Huteau & Tolu (2005). To secure adequate resolution, the computing demands were therefore significantly greater (than, for example, Gheusi *et al.* 2000), with over 10^9 mesh points used for the fine-resolution runs; this yielded over 10^7 mesh points in the wave-breaking region. The breaking wave was obtained by a suitable combination of bottom topography, domain size and F_h, chosen on the basis of the earlier literature and extensive preliminary numerical tests. These are summarised in § 2, along with details of the numerical methodology, which differs in some important respects from that of Gheusi *et al.* (2000).

In this paper, we concentrate largely on the flow *after* the breaking process is complete, so a detailed study of the transition process is not covered. However, the resolution was sufficiently high to be able to capture the transition details – starting with the appearance of Rayleigh–Taylor instabilities within the strongly sheared zone near the bottom of the characteristic 'S'-shaped region of the wave which precedes breaking. The effect of these instabilities on density contours in a y–z plane at $x = 2.5$, where $x = 0$ is the axial location of the peak of the hill (normalised by hill height), is illustrated in figure 3. Suffice it to say here that, despite the relatively high Reynolds number, there are strong similarities in the transition processes to those described by Gheusi *et al.* (2000) and Eiff *et al.* (2005), amongst others, and in particular those identified in the laboratory experiments of Eiff & Bonneton (2000), but we emphasise that the Rayleigh–Taylor instabilities identified in figure 3 have not been so well resolved previously. Afanasyev & Peltier (1998) detected similar events but with lower

https://doi.org/10.1017/jfm.2011.64 Published online by Cambridge University Press

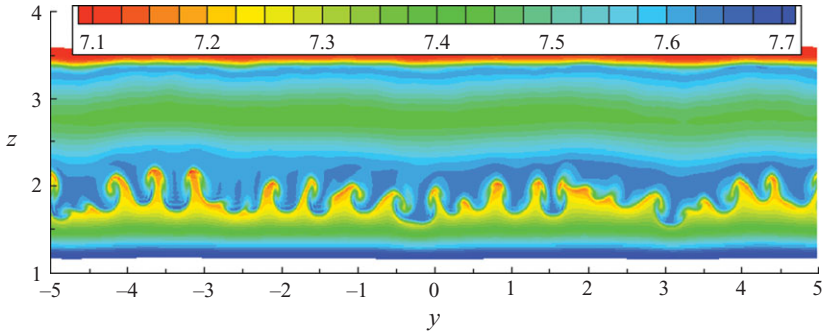


FIGURE 3. Density contours at an early stage ($t = 25$, with t normalised by hill height h and upstream velocity U) in the lower strong-shear region bordering what becomes the breaking wave, looking downstream. Here y and z are normalised by h. Transition is initiated in the downward-moving shear layer formed at the bottom edge of the lee wave. Note that the Rayleigh–Taylor mushroom-like structures contain regions of low-density (red) fluid brought into the shear layer from aloft by the downward-moving pathlines originating upstream.

resolution and they found that 'unstable layers result in formations of arrays of mushroom-like convective structures in the cross-stream direction', which appears to be a reasonable description of the visualisation in figure 3. This will all be explored in detail in a further paper but § 3 summarises the overall time development up to the appearance of the fully developed turbulent region. The major results are presented in § 4, which discusses the characteristics of the turbulence patch. Section 5 presents some further discussion and summarises the results.

2. Numerical methods

2.1. *Basic algorithms*

The DNS code originated as a finite-difference, parallel, multi-block Navier–Stokes solver, written in such a way that its efficiency generally increases with the mesh count. The earliest version of the code is described by Thomas & Williams (1997), and for density-stratified flows it was modified for the purposes of the present work to include simultaneous solution of the density equation, making the usual Boussinesq assumption. Using coordinates $x_i = (x, y, z)$, t appropriately non-dimensionalised by the obstacle height h and, for time, free-stream velocity U, the continuity, Navier–Stokes and density equations therefore become

$$\frac{\partial u_k}{\partial x_k} = 0, \tag{2.1}$$

$$\frac{\partial u_i}{\partial t} + \frac{\partial u_i u_k}{\partial x_k} = -\frac{\partial \hat{p}}{\partial x_i} + \frac{1}{Re}\frac{\partial^2 u_i}{\partial x_k^2} - \frac{\delta_{i3}}{F_h^2}\hat{\rho}, \tag{2.2}$$

$$\frac{\partial \hat{\rho}}{\partial t} + \frac{\partial \hat{\rho} u_k}{\partial x_k} = \frac{1}{ReSc}\frac{\partial^2 \hat{\rho}}{\partial x_k^2}, \tag{2.3}$$

in the usual notation, where $u_i = (u, v, w)$ and $\hat{p}$ have been non-dimensionalised appropriately using U, a reference density ρ_o (the value of ρ at the domain top) and the obstacle height h, and $\hat{\rho}$ has been normalised by $hN^2\rho_o/g$. Other quantities are dimensional unless specifically stated otherwise; $\hat{\rho}$ and $\hat{p}$ represent deviations

https://doi.org/10.1017/jfm.2011.64 Published online by Cambridge University Press

from the (hydrostatic) reference values, i.e. $\rho - \rho_o$ and $p(x, y, z, t) - p_o - \rho_o g h z$ with z directed upwards and measured from the bottom as in figure 1. Here Sc is the Schmidt number (equivalent to a Prandtl number if the scalar were viewed as temperature), characterising the ratio between the momentum and mass diffusivities, $Sc = \nu/\kappa$. Its value is of order unity in air, but around 700 in salt water. The last term in (2.2) is the buoyancy term and the only non-zero contribution appears in the vertical momentum equation of course, through the gravitational vector. Throughout this paper, we refer to t as the non-dimensional time (Ut/h) from the start of the computation. It is worth noting that if the Boussinesq assumption is *not* made, the introduction of the additional parameter (DN/U, where D is the dimensional domain height) has been shown to have significant effects on some aspects of the lee-wave motions if it is sufficiently small (e.g. Afanasyev & Peltier 1998). This may be important in some atmospheric situations (although hardly ever in oceanographic ones). It is very unlikely to affect the characteristics of the turbulence in the post-breaking patch and the present computations do not include the non-Boussinesq terms as these would unnecessarily complicate (2.2) and (2.3).

Second-order central differencing on a uniform Cartesian mesh is applied to all spatial derivatives, and a second-order Adams–Bashforth scheme is employed for time advancement using the pressure projection method. Continuity at the next time step is enforced implicitly by solving a Poisson equation for pressure using a parallel multi-grid method. Full details are given by Thomas & Williams (1997). Modification of the original code to include the density equation was performed within the existing code structure and was straightforward. Initial checks were made to ensure that computed wave modes in the general problem of the stratified flow over topography were as expected from previous theory and experiment. These were conducted for hills of various spanwise aspect ratios, in a domain of height $D = 10h$, with specified uniform upstream velocity and density gradient, zero-gradient conditions at the outlet boundary and the upper boundary representing a moving wall at the fixed upstream velocity (modelling towing tank experiments). Periodic conditions were applied at the spanwise boundaries ($y = \pm 5$) and zero-mass-flux conditions were imposed at both top and bottom boundaries for the density equation.

The obstacle was introduced impulsively into the initially uniform velocity and density gradient fields specified as upstream conditions. Many of the earlier numerical computations used a free-slip bottom boundary condition. For example, the computations of Afanasyev & Peltier (1998) illustrated in figure 2 were done in this way. The figure shows that the turbulence region originating from the breaking wave trails downstream as time increases, but this is a direct result of the free-slip lower boundary and does not occur when a bottom friction condition is used, as discussed by Richard, Mascart & Nickerson (1989) and Gheusi *et al.* (2000) for example. The present computations were undertaken with the more realistic no-slip bottom boundary condition which was assigned implicitly on the obstacle surface (as explained below), whereas symmetry (free-slip) conditions were applied elsewhere on $z = 0$. This corresponds to the lower boundary conditions used in the Reynolds-averaged Navier–Stokes (RANS) computations of Paisley & Castro (1996) and simulates the inverted experiments of, for example, Castro & Snyder (1993), where the obstacle was towed upside down at the water surface. These boundary conditions can thus be summarised by

$$u = U, \quad v = w = 0, \quad \hat{\rho} = D/h - z \quad \text{at } x = x_I \tag{2.4}$$

https://doi.org/10.1017/jfm.2011.64 Published online by Cambridge University Press

for all t and at $t=0$ (for all x, y, z)

$$\frac{\partial u, v, w, \hat{\rho}}{\partial x} = 0 \quad \text{at } x = x_E, \tag{2.5}$$

$$\frac{\partial u, v, \hat{\rho}}{\partial z} = w = 0 \quad \text{at } |x| \geqslant L/h \quad \text{and} \quad z = 0, \tag{2.6}$$

$$u = v = w = \frac{\partial \hat{\rho}}{\partial n} = 0 \quad \text{at } |x| < L/h \quad \text{and} \quad z = z_m, \tag{2.7}$$

$$u = U, \quad v = w = \frac{\partial \hat{\rho}}{\partial z} = 0 \quad \text{at } z = D/h, \tag{2.8}$$

$$u_i|_{y_E} = u_i|_{y_I}, \, \hat{\rho}|_{y_E} = \hat{\rho}|_{y_I} \quad \text{at all } x, z, t \text{ (on } y_E = -y_I = 5), \tag{2.9}$$

where L and z_m define the hill length and surface height (see below) respectively, n is the normal to the hill surface and x_I, x_E are the locations of the upstream and downstream boundaries respectively (see § 2.2). Note that the fourth of these conditions (i.e. on the hill surface z_m) was not satisfied explicitly. Rather, the immersed boundary method used to specify the hill surface (see below) yielded effectively zero velocities beneath the surface and a zero mass flux through it.

Since fine details of the flow around the bottom topography were not important, and we did not wish to compromise the high efficiency of the numerical method by moving away from uniform Cartesian grids, a fairly crude immersed boundary method was used to represent the topography: a body force term was added to the right-hand side of (2.2) and used for all cells within the bounding surface of the obstacle. This drag term was of the general form,

$$F_i = -Au_i(u_k u_k)^{p/2}, \tag{2.10}$$

where $p=1$ yields the usual quadratic drag force and A is a constant defining the 'strength' of the applied force. Choices for p and A were made after an optimisation process involving numerous runs since, for example, too small a value of A does not provide sufficient boundary disturbance to produce breaking waves whereas too large a value has serious implications for the maximum time step that can be used. The term was applied within a bottom boundary shape defined by

$$\left.\begin{aligned} z_m = 0.5\left[1 + \cos\left(\pi x \frac{h}{L}\right)\right], \quad |x| \leqslant L/h \quad \text{and} \quad |y| \leqslant (W-L)/(2h), \\ z_m = 0 \quad \text{at} \quad |x| \geqslant L/h \quad \text{or} \quad |y| \geqslant (W+L)/(2h), \end{aligned}\right\} \tag{2.11}$$

where $x = y = 0, z = z_m = 1$ defines the location of the hill summit. The two spanwise ends of the hill (i.e. at $(W-L)/(2h) \leqslant |y| \leqslant (W+L)/(2h)$, with W being the maximum spanwise width at the half-height elevation) were simply the same cross-sectional cosine-shaped profile rotated through 180° as in Castro & Snyder (1993) and Paisley & Castro (1995). Here W/L is a convenient measure of the spanwise aspect ratio of the hill.

A basic parameter in the resulting flow is the (first mode) lee-wave length, l, and as an example of these tests, figure 4 shows comparisons between relatively coarse-grid computations for an axisymmetric hill (with $Re = Uh/\nu = 100$, $p=1$), the experiments of Castro *et al.* (1983) and the values expected from linear theory, which are given by $l/h = 2\pi F_h[1 - (\pi h/D)^2 F_h^2]^{-1/2}$. (Note that spanwise aspect ratio does not affect the wavelength.) Below $F_h \approx 1$, agreement is very satisfactory but note that at higher F_h there is an underestimate of the wavelength, with an error which decreases with increasing strength of the added drag force (A). Unless A was sufficiently high, it

https://doi.org/10.1017/jfm.2011.64 Published online by Cambridge University Press

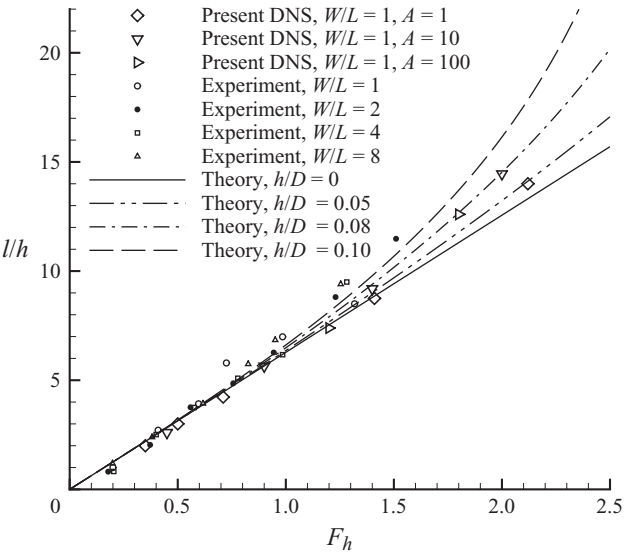


FIGURE 4. The variation of lee-wave length with F_h. Experimental data from Castro *et al.* (1983) for various spanwise aspect ratios.

was also found that for higher spanwise aspect ratio obstacles the expected wave-breaking at the lower F_h did not occur, as noted above. All the results presented below had $A = 1000$ and $p = 0$ (giving a linear drag term and replacing $p = 1$ used for some initial tests), because this yielded only very tiny velocities inside the immersed obstacle – typically $|u_i| \sim A^{-1} = 10^{-3}$ – and thus enhanced the wave-breaking effect as well as providing effective no-slip and zero-mass-flux conditions at the body surface. (The latter was checked by consideration of (2.3) on the surface.) Overall, the data from these initial stratified flow lee-wave computations provided confidence in the adequacy of the basic code.

2.2. *Sponge zones*

An important issue had to be addressed for the full, high Reynolds number, breaking-wave computations. Since very fine resolution was required for successful simulation of the breaking-wave process and the subsequent turbulent patch characteristics, it was necessary to use sponge zones so as to avoid having very large domain lengths (recall that the code uses *uniform* grids). Flows with wave breaking almost inevitably contain, in addition to the downstream waves, upstream-propagating modes. For any sensibly-sized computational domain, these would normally arrive at the upstream boundary, reflect and return to the obstacle before the wave-breaking and subsequent turbulent patch has fully developed. (This is one of the features of such flows which makes laboratory experiments difficult, particularly for two-dimensional hills for which the wave modes have their greatest strength.) The speeds of the upstream and subsequent reflected propagating modes are given by $c_u = -(K/n - 1)U$, $c_d = (K/n + 1)U$, respectively, where $K = ND/\pi U$ and n is the mode number. So, for example, for the specific $F_h = 0.6$, $D = 10h$ case discussed in this paper ($K = 5.3$), if the upstream boundary were located only at, say, $x_u = -100$ (i.e. $100h$ upstream of the obstacle crest), the first mode would arrive at that boundary after a time of only $t = 23.2$ and then reflect and arrive back at the obstacle at $t = 39.1$, which is too short a time to allow full development of the turbulent patch. The use of sponge zones to remove

https://doi.org/10.1017/jfm.2011.64 Published online by Cambridge University Press

the influence of wave reflection from boundaries is well known. We used a common approach in which additional forcing terms are introduced on the right-hand side of the governing equations (2.2) and (2.3), of the form $-\sigma(x)(q-q_r)$, where $\sigma(x)$ is a variable window function (the sponge strength); these terms 'force' the computed solution for each variable q to match the pre-computed reference solution, q_r.

A complete analysis of the efficacy of such methods has recently become available (Bodony 2006), but in the current work a somewhat *ad hoc* procedure of testing a wide range of sponge strengths and locations was used. The zones typically had a central region of constant strength, with end regions of cosinusoidal shape over which the strength smoothly fell to zero at the zone boundaries. Results were compared quantitatively with benchmark computations having boundary locations extremely remote from the hill (typically $1000h$). Such comparisons were done using relatively coarse grids, since it is the largest scales of motion which have the fastest propagation velocities and thus lead to the most serious reflection effects. Computations were done for typical cases with (i) a short domain (upstream and downstream distances of 50 or $100h$ from the hill peak) containing sponge zones (see below) and (ii) a much larger domain without such zones. Optimisation of the sponge parameters and locations led to average normalised relative errors between these two approaches of less than 1 %, up to times ($t \approx 250$) well in excess of those necessary for generation of the fully developed turbulent patch.

The results presented in the following sections were obtained using an overall domain size of $100h \times 10h \times 10h$ in the axial, spanwise and vertical directions respectively, with a two-dimensional cosine hill having $L/h = 3.56$ (see (2.11)) centred half-way between the domain boundaries at $x = 0$. Sponge zones were located between $x_I \leqslant x \leqslant x_{SI}$ and symmetrically at $x_{SE} \leqslant x \leqslant x_E$ (near the upstream and downstream boundaries, respectively), each having a $25h$ long region of cosine sponge strength given by

$$\sigma(x) = 0.5A_w\{1 + \cos[\pi(x - x_I)/(x_{SI} - x_I)]\}, \tag{2.12}$$

and

$$\sigma(x) = 0.5A_w\{1 + \cos[\pi(x - x_E)/(x_{SE} - x_E)]\}, \tag{2.13}$$

with $A_w = 0.4$, $x_E = -x_I = 50$ and $x_{SE} = -x_{SI} = 25$.

2.3. *Parameter set*

The run was performed for a two-dimensional hill at $Re = Uh/\nu = 4000$, $Sc = 1$ and $F_h = 0.6$ ($K = 5.3$) and used a time step which satisfied the advective and 'drag term' Courant conditions given by $C = |u|_{max}\Delta t/\Delta$ where $\Delta = (\Delta x \Delta y \Delta z)^{1/3}$ and (for $p = 0$) $C_{drag} = A\Delta t$, respectively. The chosen time step $\Delta t = 0.0005 = 0.5/A$ was well below about $0.15\Delta/|u|_{max}$ everywhere. This value is however much smaller than the Kolmogorov-microscale time (non-dimensional $\tau \geqslant 0.17$, with τ estimated at the point at which the dissipation was largest) – it is therefore smaller elsewhere, see § 4. Meshes had node numbers of $5120 \times 512 \times 512$ (1.34×10^9 nodes). Coarser grids were found to lead to inadequate spectra beyond the inertial sub-range, as expected, and also tended to yield rather lower maximum turbulence levels within the patch. With the fine grid used for the computations presented here, the (non-dimensional) cell sizes of $\Delta x = \Delta y = \Delta z = 0.02$ correspond to no more than three times the non-dimensional Kolmogorov scale (3.0η with, again, η estimated at the maximum dissipation point, see § 4.4); we believe this to be more than adequate for a well-resolved DNS.

https://doi.org/10.1017/jfm.2011.64 Published online by Cambridge University Press

On the (phase 1) HECToR facility at the UK's national high-performance computing service, the fine-grid runs required about 4 s per time step using 640 processor cores, with a total wall-clock time of about 150 h for a run from $t = 0$ up to $t = 67$ (via multiple restarts). About 0.4 TB of RAM was needed and typical storage requirements (depending on post-processing needs) was about 2 TB.

The 'optimal' parameter set mentioned above was chosen as a result of numerous preliminary runs (Yakovenko, Thomas & Castro 2009) with variations not only of the numerical parameters (such as time step and grid size, drag-term and sponge-layer coefficients, shapes and locations) but also geometrical parameters (spanwise and axial aspect ratios W/L and L/h) and physical ones (Re, Sc and F_h) so as to be entirely sure that the chosen parameters were the most appropriate for our purposes. In particular, a two-dimensional hill was chosen as an appropriate basic case (as in other numerical papers – Afanasyev & Peltier 1998; Gheusi *et al.* 2000) because, compared with three-dimensional hills, it leads to stronger wave-breaking over a wider range of parameters and a larger spatial area, and for longer quasi-steady periods. It also allows spanwise averaging, which maximises the accuracy of statistical quantities obtained within the turbulent patch. The hill's axial length, $L/h = 3.56$, was twice that used in the towing tank and corresponding numerical experiments (Castro & Snyder 1993; Paisley & Castro 1995, respectively), giving stronger and earlier wave-breaking activity together with a persistent mixed region at large times; further increases in L/h did not give visible enhancement of breaking. Note that $L/h = 3.56$ is close to the theoretical lee-wave wavelength at $F_h = 0.6$, which is $l/h = 3.84$ (see figure 4), so provides effective topographical tuning. The hill also has a maximum slope of 20°, close to the 21° of the Gaussian hills used by Gheusi *et al.* (2000), Eiff & Bonneton (2000) and Eiff *et al.* (2005).

The Reynolds number $Re = 4000$ was chosen after a series of coarse-grid long-time runs for a wide range of Reynolds numbers up to 20 000. Significantly smaller values give no wave overturning (for $Re \leqslant 100$) or weaker wave-breaking effects with later and shorter periods of a fully developed mixed region and clear indication of long-term periodic behaviour with quite long re-laminarisation periods, as in the DNS of Gheusi *et al.* (2000) at $Re = 200$. On the other hand, Reynolds numbers much in excess of 4000 would have required even finer meshes. Most of the data presented here used a Schmidt number of unity, but runs were also done using higher values (up to 700) and some remarks on Sc effects are given in § 5. Effects of Froude number were examined with axisymmetric hills at $L/h = 1.78$ and $Re = 100$ (as discussed earlier). Maximum wave slope was the largest for $0.6 \leqslant F_h \leqslant 0.7$ and the value $F_h = 0.6$ was chosen; for a two-dimensional hill of any shape, this is always below the critical one for wave-breaking, as shown by Castro & Snyder (1993), and is the value used by Gheusi *et al.* (2000) and Eiff & Bonneton (2000).

3. Time development up to full breaking

Typical development of the wave-breaking process is illustrated in figure 5. The first four and the last of these views (figure 5*a–d*, *g*) are snapshots of the spanwise centre-plane ($y = 0$) and at specific times from the start of the computation, which began with uniform velocity and density gradient everywhere in the field. They illustrate the way that the wave first develops the characteristic S-shaped profile seen in figure 5(*a*), having gone through the earlier stage where some streamlines become vertical, followed by a subsequent more complete convective overturning leading to the (still two-dimensional and laminar) twin vortex pair (figure 5*b*), which beyond

https://doi.org/10.1017/jfm.2011.64 Published online by Cambridge University Press

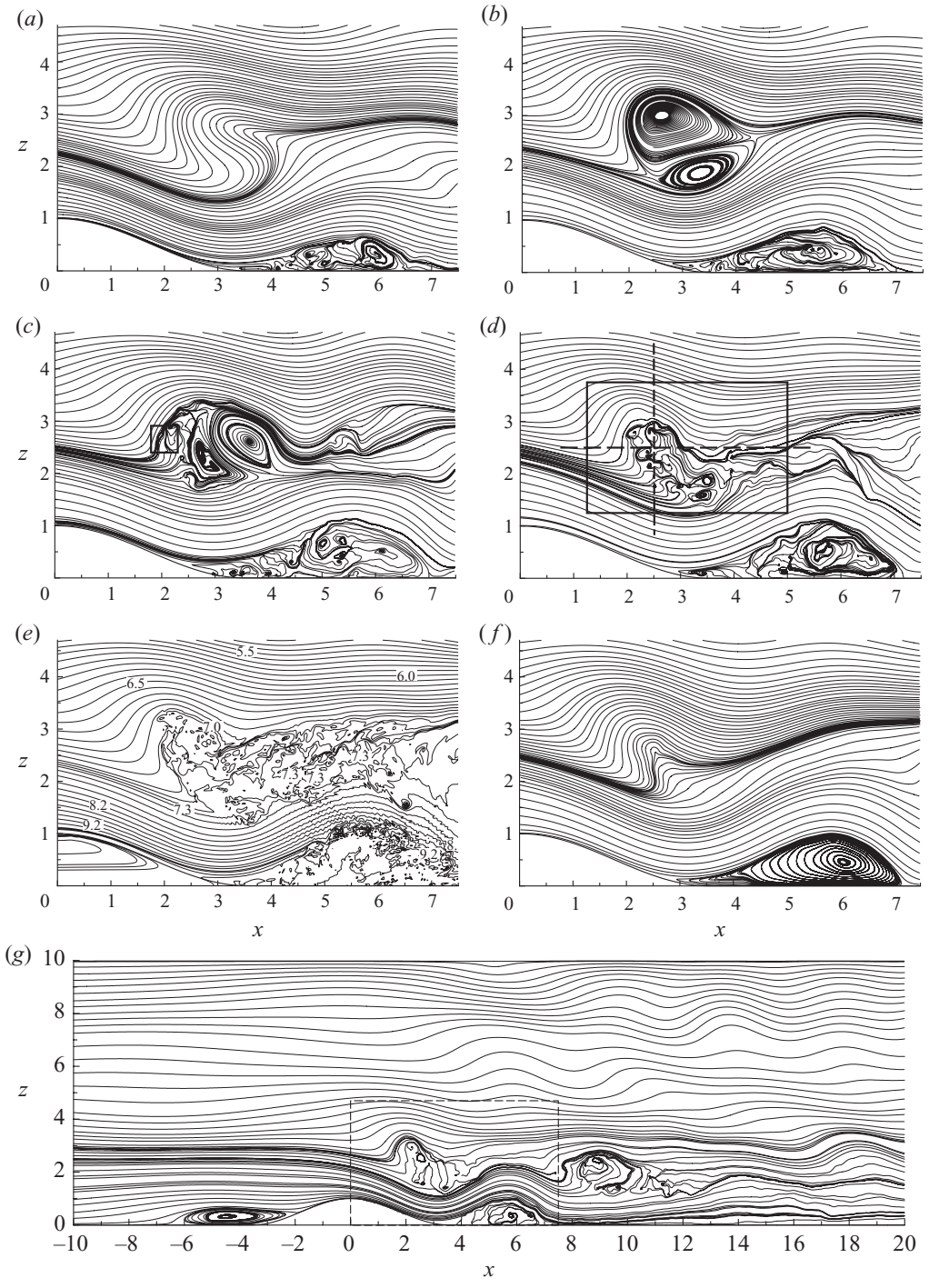


FIGURE 5. Pathlines at $t = 17.5$ (*a*), 22.5 (*b*), 27.5 (*c*) and 40 (*d*). Plot (*e*) shows density contours corresponding to (*d*). Plot (*f*) shows spanwise-averaged pathlines at $t = 40$. Plot (*g*) shows instantaneous pathlines in a larger domain at $t = 37.5$. The rectangular box in (*d*) delineates the cross-section of the averaging volume used to obtain the data in figures 7 and 13, whereas that in (*c*) shows the region used to compute the spectra of figure 8. In (*d*), the vertical dashed line at $x = 2.5$ and the horizontal dashed line at $z = 2.5$ indicate the location of the line profiles discussed in §§ 3 and 4. In (*g*), the rectangular (dashed line) box shows the boundaries of all the other views.

https://doi.org/10.1017/jfm.2011.64 Published online by Cambridge University Press

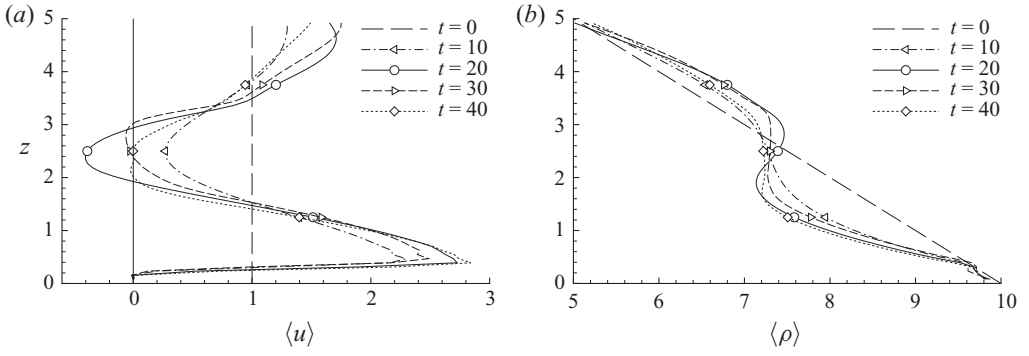


FIGURE 6. Mean axial velocity (a) and density (b) vertical profiles at $x = 2.5$, at intervals of $t = 10$.

about $t = 25$ rapidly breaks down to turbulence (figure 5c), through a process not discussed in detail here but part of which was illustrated earlier (figure 3). Subsequent snapshots naturally all look rather different within the turbulence patch, but not very different elsewhere – figure 5(d), for $t = 40$, provides an example. Figure 5(e) shows the instantaneous density field at $t = 40$, which emphasises that significant mixing has occurred by this time, even within the 'wake' of the turbulence patch. Since the hill was two-dimensional, spanwise averaging over the whole domain could be performed to determine the mean flow and figure 5(f) shows the result of such averaging at $t = 40$, so can be compared with figure 5(d) to see the typical differences between the mean and instantaneous flows. To help put these views into perspective, a snapshot of the pathlines at $t = 37.5$ over a much larger part of the domain is shown in figure 5(g), illustrating the presence of a second breaking region some way downstream of the main patch, generated in a somewhat similar fashion roughly one (initial) lee-wavelength downstream of the latter. Similar second or even multiple wave-breaking has been observed in experiments but is often both less steady and sometimes smaller; this region was not studied in detail.

Figure 5 also illustrates the downwind rotor – a separation bubble similar to that in the near-wake behind an obstacle – apparent in the region $3 < x < 7$, $z < 1$. This is caused by boundary-layer separation occurring because of the strongly adverse axial surface-pressure gradient linked to the trapped lee wave. It is highly turbulent and appears (in time) well before the elevated turbulent patch. Because it is a result of a separating boundary layer, it is not present in computations with a free-slip obstacle surface (Richard *et al.* 1989; Gheusi *et al.* 2000). There is also an upstream separation region evident in figure 5(g), which was very unsteady, disappearing at some times or becoming turbulent. In this case, the adverse pressure gradient which causes it is not linked directly to the lee waves, but is simply a result of the hill itself.

A more quantitative way of tracking the development of the turbulence is to consider the behaviour in time of turbulence quantities. Figure 6 shows, as an example, mean velocity and density profiles at $x = 2.5$ (averaged as explained in § 4.2, (4.2)) for times prior to the appearance of the fully developed turbulent patch. Note in particular how the profiles overshoot their eventual form – the $t = 40$ data are an example of that eventual form (see figure 10, discussed later). At $t = 20$, the density profile (figure 6b) has the 'S' shape characteristic of the flow shown in figure 5(a, b), prior to the appearance of any instabilities, and the minimum axial velocity is strongly

https://doi.org/10.1017/jfm.2011.64 Published online by Cambridge University Press

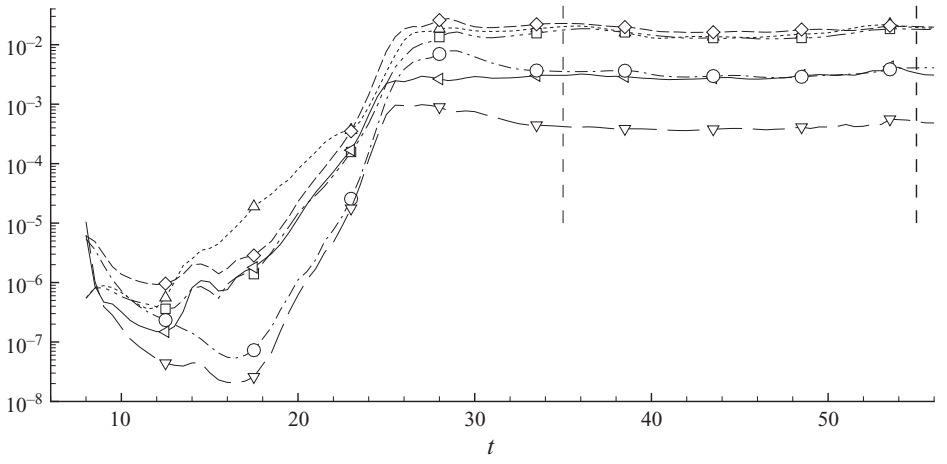


FIGURE 7. Time variation of the spatially averaged normal Reynolds stresses and scalar (density) variance within a box covering the breaking region (see figure 5*d*). Symbols: △, $\langle u'^2\rangle$; □, $\langle v'^2\rangle$; ◇, $\langle w'^2\rangle$; ◁, $\langle \hat{\rho}'^2\rangle$; ○, ϵ; ▽, $\epsilon_\rho = 2\langle(\nabla\hat{\rho}')^2\rangle/(ReSc)$. The last two are dissipation terms in the turbulent kinetic energy (see § 4.3) and scalar variance balances, respectively. All functions are normalised as appropriate (see § 2.1). Vertical dashed lines indicate the extent of the quasi-steady period.

negative (figure 6*a*). The subsequent transition process removes the large convectively unstable region of the density profile and reduces the total velocity deficit.

It should be noted that to reduce the necessary computational times, the transition process was accelerated by using white-noise seeding to break the two-dimensional flow symmetry. This seeding was applied to the entire density field at $t = 7.5$ and had an amplitude of 2 % of the initial background density change over the obstacle height. The initial perturbation generated by the seeding gradually decays and the flow remains laminar until about $t = 20$, before energy is rapidly extracted from the remaining noise and seeds the inherent three-dimensional instability having a (spanwise) wavelength of $0.5h$ (by $t = 25$), leading to the Rayleigh–Taylor signature seen in figure 3. Without such explicit seeding, the transition process would be initiated very much later (relying merely on numerical noise for its seeding). A similar technique was employed by Gheusi *et al.* (2000), although they applied a much higher amplitude seeding, restricted to only part of the domain.

Figure 7 shows the three normal Reynolds stresses, the second moment of the scalar fluctuations, and the dissipation of the turbulent kinetic energy and scalar fluctuations, obtained by spatially averaging the data in a region defined by $1.25 \leqslant x \leqslant 5$, $-5 \leqslant y \leqslant 5$, $1.25 \leqslant z \leqslant 3.75$, i.e. in a spanwise rectangular box of cross-section $3.75h \times 2.5h$ in the vertical plane and thus covering the entire breaking region; the box is shown in figure 5(*d*). Such averages – of the axial stress component for example – are defined by

$$\langle u'^2\rangle(t) = \frac{1}{V}\int_{-5}^{5}\int_{1.25}^{5}\int_{1.25}^{3.75}(u(x', y', z', t) - \langle u(x', z', t)\rangle)^2 \mathrm{d}x'\mathrm{d}z'\mathrm{d}y', \qquad (3.1)$$

in which V is the volume of the box (93.75) and the mean value $\langle u(x, z, t)\rangle$ is computed by averaging over y only. (Note that in order to minimise errors, the order of the averaging – the y-direction first, followed by the x-, z-directions after obtaining the deviations from the mean values – is important.) The flow within this region

https://doi.org/10.1017/jfm.2011.64 Published online by Cambridge University Press

remains laminar until beyond $t = 20$, but then rapidly goes through transition before settling into an approximately steady state during the period $35 \leqslant t \leqslant 55$ after some initial overshoot behaviour at earlier times. It is this quasi-steady-state period which is discussed in the following section. Note that it is quite long: $\Delta t = 20$ corresponds to the order of at least an hour in a typical atmospheric situation of a 10 $\mathrm{m\,s^{-1}}$ wind flowing over a 2 km high ridge – see for example Ying & Baopu (1993), who simulated the Boulder windstorm of 1972 originally discussed by Klemp & Lilly (1977). Although the log scale used does not make it very obvious, a close look at the data beyond $t \approx 52$ shows that the stresses rise somewhat. This is almost certainly due to the gradual rise (and slight shape changes) of the entire turbulent patch, so that the upper and downstream regions of the box shown in figure 5(d) also become turbulent. (Recall that the stresses are averaged over the entire box.) Note also that in the early transitional period, the (seed) density fluctuations introduced at $t = 7.5$ first fall before triggering the transition process. Once the Reynolds stresses have risen to levels within an order of magnitude of their fully turbulent values (around $t = 24$), it is the vertical normal stress, $\langle w'^2 \rangle$, which rises most rapidly, feeding energy to the other components. Gheusi *et al.* (2000) found similar behaviour even at their very much lower Reynolds number ($O(100)$). Moreover, the scalar fluctuations $\langle \hat{\rho}'^2 \rangle$ grow in the same manner as the spanwise and vertical velocity fluctuations ($\langle v'^2 \rangle$ and $\langle w'^2 \rangle$) during $14 < t < 25$, and likewise the two dissipations vary very similarly over the same period. Another interesting feature is that during the quasi-steady period, the ratio between the velocity and scalar dissipation (discussed in more detail in § 4.3.1) is roughly the same as that between the velocity and scalar fluctuations themselves.

4. Characteristics of the turbulent patch

4.1. *Initial remarks*

A genuinely steady turbulent patch was not anticipated. Even if the turbulence characteristics within both itself and the strong shear layers around its boundaries were such as to allow a turbulent kinetic energy balance constant in time – i.e. $\partial k/\partial t = 0$ – it is known that these lee-wave systems are not steady, even if the conditions far upstream remain fixed. This was first noticed in the laboratory by Castro, Snyder & Baines (1990) and subsequently explained on the basis of linear theory by Rottman, Broutman & Grimshaw (1996), who showed that (for sufficiently short obstacles and in the present parameter range) there is a very-long-time-scale periodic oscillation of the lee-wave system, which persistently generates upstream-propagating waves. The period of these oscillations was found to be very close to those measured in the laboratory. Although they did not realise it, this is almost certainly the cause of what Gheusi *et al.* (2000) called an 'intermittent phenomena' in their low-Reynolds-number computations of a case similar to the present one. The time scale they noted fits very well to that predicted by Rottman *et al.* (1996).

In this paper, we do not consider this longer-time-periodic evolution, tracking the cycle of appearance, disappearance and re-appearance of the turbulent patch; the eventual process which leads to decay of the turbulence in the patch is therefore not explored in detail. Computational requirements would be very large if this were to be attempted using the very fine grid employed in the present computations. However, some coarser grids were used in order to reach longer times and the results showed that the patch does indeed eventually disappear, being replaced by a lower-amplitude wavetrain similar to that seen at very much earlier times. The waves then steepen and break and the whole process would (presumably) be repeated if the computations

https://doi.org/10.1017/jfm.2011.64 Published online by Cambridge University Press

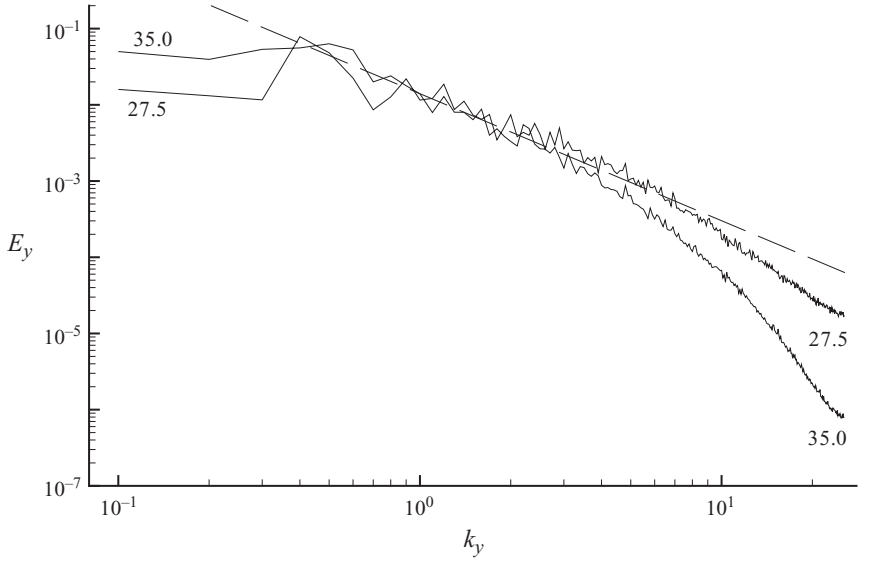


FIGURE 8. TKE spectra in the spanwise direction, averaged over the small box of side $h/2$ shown in figure 5(c); labels refer to t values. The dashed line has a slope of $-5/3$.

were continued for long enough times. Note that some long-time runs (with the coarser grid) showed that full relaminarisation in the wave-breaking region did not occur, or at least not until beyond $t = 225$ by which time the sponge layer had become less reliable, as judged by the initial tests discussed in § 2.2. Not surprisingly, the full relaminarisation between the quasi-steady patch periods happens more easily at low Reynolds numbers, as the $Re = 200$ experiments showed (Gheusi *et al.* 2000). Our focus here is on the nature of the turbulent patch during the quasi-steady period and because the time scale for the long-term periodicity is so long – well in excess of the quasi-steady period in the present case – it is indeed reasonable to consider the turbulent patch as quasi-steady on time scales much less than this and perform time averages over these shorter times in order to obtain useful statistics.

For the remainder of the paper, we proceed on that basis, considering the turbulent patch to be fully developed and steady beyond $t = 35$ (and up to $t = 55$), as suggested by the data in figure 7. Figure 8 illustrates a further reason why we believe $t = 35$ is a sensible starting time to choose. Spatial spectra of the turbulent kinetic energy (TKE) as a function of the spanwise wavenumber $k_y = h/\lambda_y$ are shown for $t = 27.5$ and 35. These were obtained by averaging over a small box in the x–z plane, of side $0.5h$ and centred at $x = 2.05$, $z = 2.65$, i.e. near the front of the breaking region (see figure 5c). As shown in § 4.3, this region has the highest levels of turbulent kinetic energy (and production and dissipation). At $t = 27.5$, there is a significant low-wavenumber peak around $k_y = 0.4$, which corresponds to a spanwise wavelength of $\lambda_y = 2.5h$. This is very close to the wavenumber associated with the vortex structures discussed in earlier work (e.g. Gheusi *et al.* 2000), but note that in the present case the development of the latter is preceded by the Rayleigh–Taylor instabilities illustrated in figure 3 (having a typical spanwise wavelength around $0.5h$), which seem not to have been so clearly identified previously (but see Voropayev, Afanasyev & van Heijst 1993; Afanasyev & Peltier 1998). At $t = 35$, however, no remnant of any of these structures remains, at least at this x, z location, and the spectrum is thus essentially flat at low wavenumber, as figure 8 shows. The spectra also contain at least a decade of reasonable $-5/3$

https://doi.org/10.1017/jfm.2011.64 Published online by Cambridge University Press

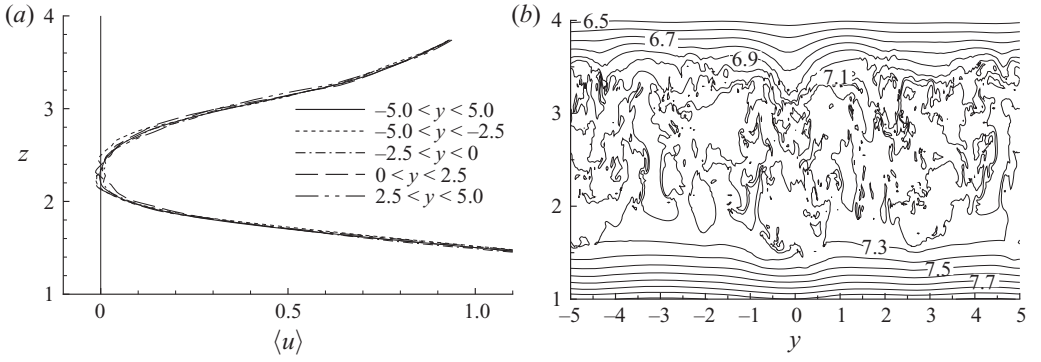


FIGURE 9. (*a*) Vertical profiles of mean axial velocity at $x = 2.5$, averaged over $35 \leqslant t \leqslant 55$ and over the four quarter-span widths and the entire span. (*b*) Instantaneous density contours in the spanwise vertical plane at $x = 2.5$ and $t = 35$.

inertial subrange behaviour, immediately suggesting that buoyancy effects have an insignificant effect on the turbulence within this region. Deviations from this spanwise spectrum at later times are insignificant so the inertial sub-range exists throughout the quasi-steady period, as well as in other areas of the turbulent patch.

Eiff & Bonneton (2000) and Gheusi *et al.* (2000) identified dominant structures with periods in the range $\lambda_y/h = 2.4$ to 4. However, their Reynolds numbers were typically only around 200. In view of the present case of much higher Reynolds number, such structures, even if they existed, would have been heavily modulated by the smaller scales resolved in the computations. There was certainly no clear sign of them (above the inevitable scatter at low wavenumbers) in any of the spectra we computed for $t \geqslant 35$. Note that since the spectral energy at zero (spatial) wavenumber, $E_y(0)$, can be expressed as $4\langle u'^2\rangle L_{uy}/h$, where L_{uy} is the lateral integral scale of the axial velocity component, the flat region of the $t = 35$ spectrum can be used to deduce that $L_{uy}/h = 0.45$; the spanwise integral scale is thus somewhat smaller than the depth of the patch, emphasising the fully three-dimensional nature of the turbulence by this stage.

4.2. *Mean flow and Reynolds stresses*

Averaging over the entire span was used for all the results presented in this section, in order to reduce scatter and to exploit the two-dimensionality of the mean flow (recall that the hill is two-dimensional). This is only meaningful, of course, if the time-averaged mean flow is genuinely two-dimensional and the data in figure 9 are shown first as confirmation of that. Profiles of axial mean velocity through the patch at $x = 2.5$, averaged over the quasi-steady period and various spanwise widths, are presented in figure 9(*a*). In this figure, the mean velocity $\langle u\rangle$ is therefore defined by

$$\langle u\rangle(x, z) = \frac{1}{20(y_2 - y_1)} \int_{y_1}^{y_2} \int_{35}^{55} u(x, y', z, t')\,\mathrm{d}y'\,\mathrm{d}t'. \tag{4.1}$$

The profile is virtually independent of whether all or some of the span is used for the averaging. Figure 9(*b*) shows instantaneous density contours on a vertical plane at $x = 2.5$; this view is typical of snapshots at any time within the quasi-steady period and although, at the top and bottom edges of the patch, some faint spanwise periodicity might be deduced, it is heavily modulated and there is certainly

https://doi.org/10.1017/jfm.2011.64 Published online by Cambridge University Press

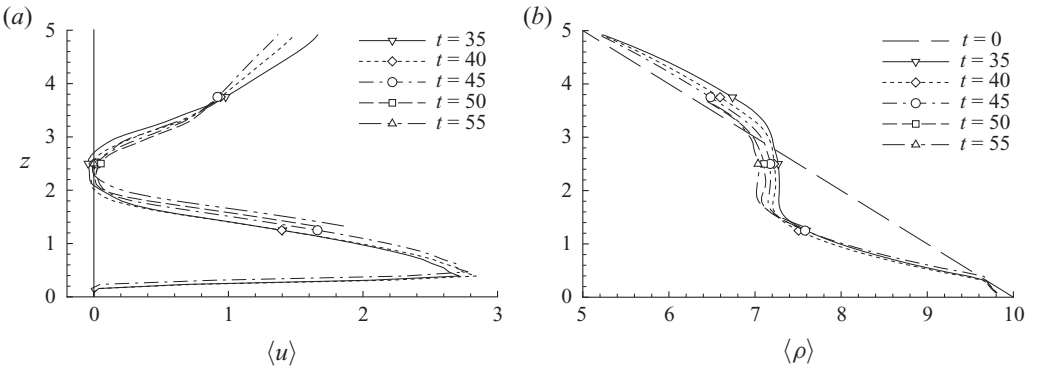


FIGURE 10. (*a*) Mean axial velocity and (*b*) density vertical profiles at $x = 2.5$, at five times during the quasi-steady period.

no evidence of spanwise periodic structures within the patch. Many similar results were collected and we are confident that the mean flow is essentially two-dimensional. (Note, however, that some evidence of spanwise structures was apparent in the coarser grid computations not only during the transition stage, as expected, but also during the much later transition towards patch relaminarisation.)

Before considering the global characteristics of the turbulent patch, whole-span averages at various times within the quasi-steady period were computed. To reduce scatter, these were obtained by additional averaging over small x–z areas of $0.16h \times 0.16h$ (containing 64 cells), so the quantities shown are defined by relations such as

$$\langle u\rangle(x, z, t) = \frac{1}{0.16^2 \times 10} \int_{-5}^{5} \int_{x-0.08}^{x+0.08} \int_{z-0.08}^{z+0.08} u(x', y', z', t)\, \mathrm{d}x' \mathrm{d}z'\, \mathrm{d}y'. \qquad (4.2)$$

Figure 10 shows vertical profiles of axial velocity and density at $x = 2.5$ (this location is identified in figure 5*d*) and at five times. The mean density deviation $\langle\rho\rangle = \langle\hat{\rho}\rangle$ was defined using the reference density ρ_o assigned at the top of the domain so that initial upstream density deviations are positive – $0 \leqslant (\hat{\rho}|_{t=0} = \hat{\rho}|_{x=x_I} = 10 - z) \leqslant 10$. Note first that there is a slow but noticeable drift in these profiles, corresponding to a gradual rise of the turbulent patch as mentioned earlier. However, this does not affect the main features of the profiles. These show a well-mixed (nearly constant density) region identifying the main patch lying between $z \approx 1.5$ and $z \approx 3$, within which the axial velocity is only close to zero in a restricted central region. The shear layers immediately above and below this region are of uniform density, but extend into regions where the density gradient is negative (stabilising). Figure 10(*b*) includes the initial background density profile and it is evident that below the fully mixed region, the density field is much more strongly stable than it was initially. This is linked directly to the 'trapping' nature of the broken wave and subsequent turbulent patch, with the generation of strong downslope winds, widely discussed elsewhere (e.g. Smith 1985; Scinocca & Peltier 1993). Note that the maximum axial velocity in the near-surface region reaches almost three times the upwind approach velocity, before falling back towards zero through the boundary layer on the obstacle surface. Note also that the rapid changes in velocity and density gradient near $z = 0.4$ are close to the edge of the surface boundary layer and may not be fully resolved, but this region is far from the wave-breaking region, so improved resolution here was not required.

https://doi.org/10.1017/jfm.2011.64 Published online by Cambridge University Press

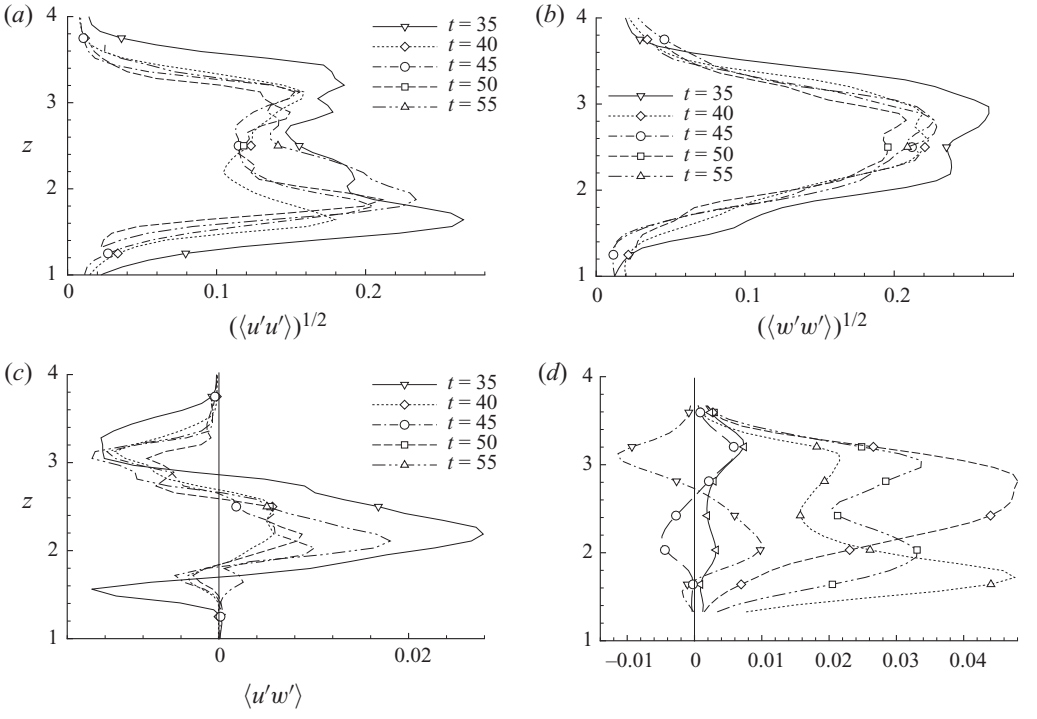


FIGURE 11. (*a*) Axial and (*b*) vertical intensity profiles and (*c*) shear-stress profiles at $x = 2.5$ at five times within the quasi-steady patch period. (*d*) Reynolds stress and flux profiles averaged over the entire patch period, $35 \leqslant t \leqslant 55$, at $x = 2.5$; symbols: △, $\langle u'^2 \rangle$; □, $\langle v'^2 \rangle$; ◇, $\langle w'^2 \rangle$; ▽, $\langle u'w' \rangle$; ◁, $\langle \hat{\rho}'^2 \rangle$; ○, $\langle w'\hat{\rho}' \rangle$.

Incidentally, the rapid changes are not discontinuities; without the x, z-averaging, the profiles would contain significant scatter. Note also that the obstacle surface at this location is near $z = 0.2$; zero velocities for $z < 0.2$ (as also seen in figure 6) simply emphasise the adequacy of the implicit no-slip condition at the surface.

Reynolds stresses corresponding to the profiles of figure 10 are shown in figure 11, computed in a similar manner. The normal stresses are plotted as turbulence intensities, e.g. $\langle u'^2 \rangle^{1/2}$, to emphasise the high levels of turbulence within the patch. If they were normalised by the local velocity (figure 9*a*) rather than U, the true local intensities would be even higher than the peak values of around 0.2. Note that in the experiments of Eiff *et al.* (2005) (at $Re = 9000$), the intensities also reach about 20 % at some points within the turbulent patch. The spanwise component is not shown but has magnitudes similar to the axial stress, whereas the vertical stress is a little higher than these. In spite of the slight scatter, which might be expected since no time-averaging was used, there is reasonable agreement at all times, except perhaps for noticeably larger Reynolds shear-stress magnitudes at the earliest time ($t = 35$), compared with later times (figure 11*c*).

Figure 11(*d*) shows all the stresses at $x = 2.5$, averaged over the quasi-steady period of the patch (so using the stress relations corresponding to (4.2) but with an additional integral over the 20 time units, performed *after* both the spanwise y-integration and the x, z-integration, to avoid non-turbulent contributions caused by the slight drifting of the patch location with time). The most obvious collective feature of all profiles is

https://doi.org/10.1017/jfm.2011.64 Published online by Cambridge University Press

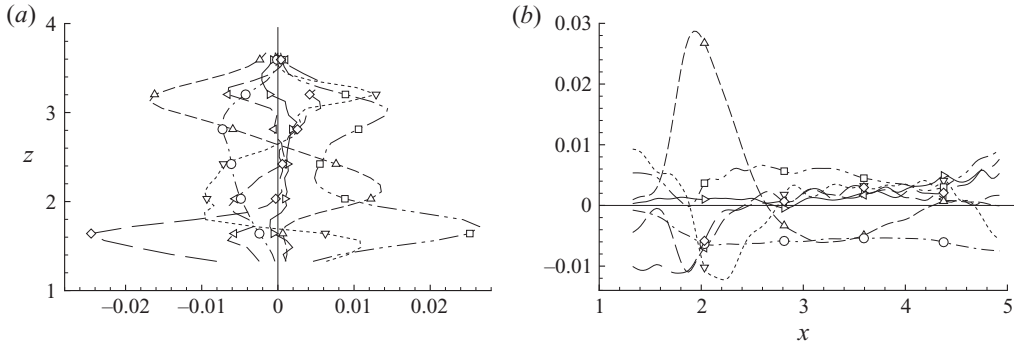


FIGURE 12. TKE balance averaged over $35 \leqslant t \leqslant 55$, along (*a*) $x = 2.5$ and (*b*) $z = 2.5$. Symbols: $\triangleright$, k_t; $\triangledown$, $D_t + D_v$; $\triangleleft$, D_p; $\square$, P_k; $\triangle$, G_k; $\bigcirc$, $-\epsilon$; $\diamond$, $-A_k$.

their (rough) qualitative similarity to what would be expected in a two-dimensional classical plane turbulent wake (Townsend 1976). For example, the peak shear-stress locations correspond roughly to the locations of the maximum mean velocity shear and moreover there is even a hint of two peaks in the horizontal stress components, just as usually seen in plane wakes. In such wakes, the maximum values of the normal and shear stresses are typically around $0.15U_d^2$ and $0.05U_d^2$, respectively, where U_d is the maximum mean velocity deficit. To be quantitatively consistent with the present data, this requires an equivalent U_d of about $0.5U$, which is perhaps rather smaller than what might be straightforwardly estimated from the mean velocity profiles in figure 9(*a*). However, it is well known that wake profiles are in fact significantly dependent on initial conditions, contrary to Townsend's classical assumptions (see Zhou & Antonia 1995, for example), and there is little reason to suppose that in the present case, quantitative values would match those in classical (far-field) wakes. Certainly, the initial conditions leading to generation of the patch are very different from those generating classical planar wakes but, in fact, initial regions of negative axial velocity are common to both and the profiles are not dissimilar to those in *near*-field wakes behind two-dimensional generating bodies (e.g. a cylinder). The analogy with plane wakes, whilst interesting, should obviously not be taken too far however.

4.3. *The turbulent kinetic energy balance*

4.3.1. *Global considerations and mixing*

Requirements for a roughly steady turbulent patch include no net (spatially averaged) excess of production over dissipation of turbulence energy and that around its boundaries there should be no net transport of turbulence into or out of the patch. It is also of interest to know the relative contributions of energy production through buoyancy and shear. These questions are first addressed by considering the TKE balances shown in figure 12, along $x = 2.5$, $z = 2.5$. As in the case of the profiles shown in figure 11(*d*), each term was obtained by averaging in the spanwise direction and over small x, z areas of $0.16h \times 0.16h$, then over the period of the turbulent patch. Note that P_k, G_k, ϵ and A_k denote the shear production, buoyancy production, dissipation and advection terms, respectively, D_t and D_v (not shown separately) denote the turbulent transport (by triple-velocity products) and the viscous diffusion, respectively, and D_p is the turbulent transport by pressure fluctuations. The latter process is in many flows very small compared with triple-velocity turbulent transport (D_t), but in the present flow could, in principle, be significant not least because

https://doi.org/10.1017/jfm.2011.64 Published online by Cambridge University Press

stratified shear layers can be a source of internal wave generation. The various terms are defined by

$$P_k = -\langle u_i' u_j' \rangle \frac{\partial \langle u_i \rangle}{\partial x_j}, \tag{4.3}$$

$$G_k = -F_h^{-2} \langle \hat{\rho}' w' \rangle, \tag{4.4}$$

$$\epsilon = Re^{-1} \left\langle \left(\frac{\partial u_i'}{\partial x_j} \right)^2 \right\rangle, \tag{4.5}$$

$$D_t = -\frac{\partial \langle u_i' u_j' u_j'/2 \rangle}{\partial x_i}, \tag{4.6}$$

$$D_p = -\frac{\partial \langle u_i' \hat{p}' \rangle}{\partial x_i}, \tag{4.7}$$

$$D_v = Re^{-1} \frac{\partial^2 k}{\partial x_i^2}, \tag{4.8}$$

$$A_k = \langle u_j \rangle \frac{\partial k}{\partial x_j}, k = \langle u_i' u_i' \rangle /2, \tag{4.9}$$

in the usual notation and with all coordinates and quantities normalised as explained in § 2. (Dashes denote fluctuating quantities and angled brackets denote means averaged at least over the span, e.g. $u_i' = u_i - \langle u_i \rangle$. Thus, although the turbulence quantities contain contributions from all waves and instabilities, any wave motions with inherent spanwise wavelengths are averaged out.) The balance can be expressed by

$$m = -\frac{\partial k}{\partial t} - A_k + P_k + D_t + D_p + D_v = -G_k + \epsilon, \tag{4.10}$$

where m is the net mechanical energy required to sustain the turbulent motions (Ivey & Imberger 1991). Here G_k, the buoyancy flux, is positive if it represents a gain in TKE (as the shear-stress production term normally does). Except for the residual determination of $\partial k/\partial t$, all items of the transport equation (4.10) were directly calculated from the computational data, with the assumption that the patch was essentially two-dimensional, i.e. inhomogeneous only in the x–z plane. This reduced the computational effort since some terms in the full expressions (e.g. (4.3)) then become identically zero. Note that $\partial k/\partial t$ was approximated by the residual value (denoted by k_t) of the computed balance of all the other terms (as also done by, for example, Dornbrack 1998), so any numerical errors in computation of the discretised forms of (4.3)–(4.9) were implicitly included in it. Since it seems very unlikely that the numerical errors were, fortuitously, large and of opposite sign to the real $\partial k/\partial t$, thus giving the generally small value of the balance term (see figure 12), we deduce that the numerical errors were in fact very small. (Second-order differencing was employed to deduce all the terms, consistent with the order of the original discretisation of (2.1)–(2.3), and the spatial-/time-averaging was based on more than 10^6 values for each quantity shown in figure 12, so there is no reason to expect significant numerical errors.)

The viscous diffusion D_v was negligible everywhere compared with the other terms but for completeness is included in figure 12 summed with the turbulent transport term D_t. The main features of figure 12(a) are evident. Buoyancy production has peaks not dissimilar in magnitude to the shear production peaks which occur around the regions of maximum mean velocity gradient, as expected. Figure 12(b) suggests, however, that

https://doi.org/10.1017/jfm.2011.64 Published online by Cambridge University Press

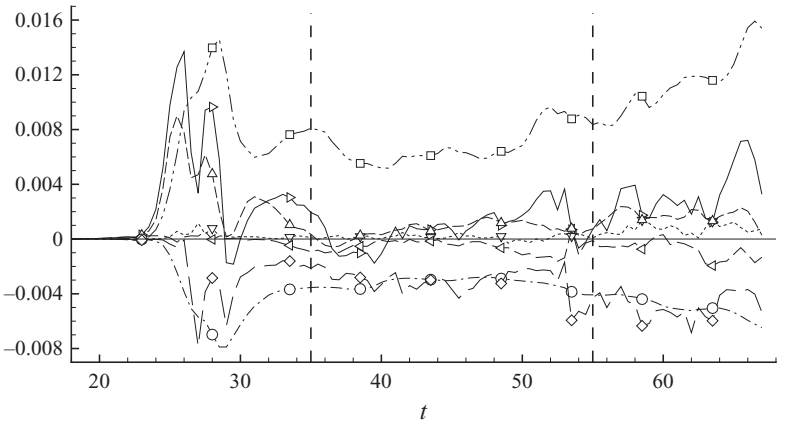


FIGURE 13. Global TKE balance averaged over the turbulent patch (i.e. the box shown in figure 5*d*). Symbols: $\triangleright$, k_t; $\triangledown$, $D_t + D_v$; $\triangleleft$, D_p; $\square$, P_k; $\triangle$, G_k; $\bigcirc$, $-\epsilon$; $\diamond$, $-A_k$.

these peaks become much less prominent further downstream in the patch. However, $x = 2.5$ is a location typical of the front of the patch where G_k can have either sign; it provides a source of energy towards the bottom of the patch (around $z = 2$) and a sink near the top (around $z = 3.2$). The overall G_k distribution is discussed in more detail later, but reference to figure 14(*b*) will immediately illustrate the size and location of the small regions of significant buoyant production or destruction of turbulent kinetic energy. Note that the *only* region in or around the patch where the buoyancy flux is negative is centred around $x = 2.6$, $z = 3.0$ and is discussed further below.

Figure 12(*a*) suggests that there is significant transport of kinetic energy upwards into the central region of the patch by the mean flow at its lower boundary (A_k reaches values around 0.025 at $z = 1.6$) but, again, this weakens further downstream. The vertically integrated sum of total production and dissipation (which would balance in a homogeneous flow) is positive, advection providing the additional necessary sink of energy. Overall, there is an approximate balance of all terms (4.3)–(4.9) along the plane $x = 2.5$, indicated by the fact that $k_t \approx \partial k/\partial t \sim 0$ (figure 12*a*). The latter is only significant in the downstream wake (figure 12*b*), where the positive values are caused by advective transport from areas near the front and lower boundaries of the patch (see also figure 14*g*, discussed below). A final point to emphasise concerns the behaviour of the pressure transport term, D_p. At $x = 2.5$ (figure 12*a*), this is only significant near the top and bottom of the patch and represents a sink of energy. A little further upstream, it becomes slightly larger around the front of the patch (see later) and it is probable that the stratified shear layer in that region is a continual weak source of internal waves, which have been shown previously to lead to additional removal of turbulent kinetic energy as they propagate (Pham, Sarkar & Brucker 2009).

These single-line profiles cannot, of course, clarify the global (patch-averaged) characteristics. Figure 13 shows the various TKE balance terms averaged over the patch region (as shown in figure 5*d* and used earlier in figure 7 with the formulation in 3.1), as a function of time. Its most important feature is that during the quasi-steady period, the net buoyancy production is relatively small (although there is perhaps a weak tendency for it to rise slowly with time). There is thus quite a close balance between production of turbulence energy by shear and its removal by dissipation and advection (P_k, ϵ, A_k respectively). Turbulent transport (through both triple product

https://doi.org/10.1017/jfm.2011.64 Published online by Cambridge University Press

Location/term	$-k_t^n$	$-A_k^n$	P_k^n	D_t^n	D_p^n	$-G_k^n$	ϵ^n
Global (over whole patch)	−0.30 Si	−1.21 Si	2.68 So	0.05 So	−0.22 Si	−0.26 So	1.26 Si
$x=2.5, z=3.2$	0.05 –	0.20 So	0.43 So	0.64 So	−0.32 Si	+0.79 Si	+0.21 Si

TABLE 1. Values of terms in the kinetic energy equation (4.10) normalised by $m=-G_k+\epsilon$. Labels under each value indicate whether the term is a source (So) or sink (Si) of TKE. The sum of the first five terms (unity) must equal the sum of the last two, see (4.10).

gradients or pressure diffusion) is very small and the residual balance term, $k_t \approx \partial k/\partial t$, is also small during the quasi-steady period – $35 \leqslant t \leqslant 55$. (Note that the ϵ data are also shown in figure 7.) The temporal evolution of the TKE balance terms shown in figure 13 is similar to that found by Dornbrack (1998) in LES of breaking waves: TKE integrated over the domain grew rapidly during the transition stage, initially by buoyancy and later by shear production, but during the quasi-steady period, the positive shear production and the negative contribution from dissipation were balanced and the temporal change of TKE was almost zero.

A summary of the relative size of the various terms in the TKE equation, averaged over the whole patch and then over the quasi-steady period, is provided by the data in table 1. Here, the 'global' values of all terms have been normalised by the 'global' value of m (4.10). When the buoyancy term G_k is negative, it provides an additional energy sink. Globally, however, over the quasi-steady period, G_k is in fact positive, although it is only about 9 % of the total production of TKE (P_k+G_k) and 10 % of P_k alone, so contributes relatively little to sustaining the TKE within the patch. We emphasise that within the fully mixed region, buoyancy processes are not significant at all; typical density fluctuations are not small (the correlation coefficient between ρ' and w' ranges between about ± 0.5, for example, as deduced from the data in figure 11*d*), but the mean density gradient is close to zero (figure 10*b*) and the density fluctuations have no large-scale dynamical significance. Around the edges of this fully mixed region, however, there are significant (negative) density gradients. Near the bottom of the mixed region, the buoyancy flux is an energy source but, as noted above, near the top it is a sink – at $x=2.5, z=3.2$ for example (see the negative peak there in G_k in figure 12*a*). Table 1 includes further normalised data obtained at a location in this region and it is evident that here the buoyancy flux accounts for about 75 % of total dissipation m and, indeed, is significantly larger numerically than the shear production. Here the axial velocity shear is strongly positive (figure 10*a*) and there is a strong negative density gradient (figure 10*b*). The relatively large (and negative) flux Richardson number commonly defined by $R_f=G_k/P_k$ ($=-1.8$ at the $x=2.5, z=3.2$ location) contrasts with the globally positive value (≈ 0.10), mirrored over practically all of the rest of the patch. Such contrasts are symptomatic of gravity wave 'mediation of the transfer of kinetic energy from the mean flow to the turbulence' (Smyth *et al.* 2001). From the first line of table 1, one can also see that globally $|D_t| \ll |D_p|$. This is similar to the DNS results of Pham & Sarkar (2010) for a stably stratified jet with radiation of internal waves, where D_v is negligibly small and D_t is significant only in the shear layer regions, whereas the pressure transport D_p is the largest component of the total transport ($D_t+D_v+D_p$) in the far jet and at early times in the near jet.

https://doi.org/10.1017/jfm.2011.64 Published online by Cambridge University Press

It is also of interest to consider the geophysically important concept of 'mixing efficiency'. Different authors use rather different definitions of this. Ivey & Imberger (1991) considered a generalised flux Richardson number defined by $-G_k/(\epsilon - G_k)$, which globally within the turbulent patch is about 0.26 (see table 1). On the other hand, Pham *et al.* (2009) and Pham & Sarkar (2010), for example, use the ratios of buoyancy flux and scalar dissipation to TKE dissipation, $\Gamma = G_k/\epsilon$ and $\Gamma_\rho = \epsilon_\rho/\epsilon$ respectively, as more conventional measures of momentum and scalar mixing efficiencies. Globally, the data in table 1 yield a value $\Gamma = 0.2$, which is exactly the constant value taken in many oceanographic applications (e.g. Smyth, Hebert & Moum 1996). Figure 13 also suggests that Γ varies in time within the quasi-steady period (from -0.16 at $t = 36.5$ to 0.57 at $t = 47.5$, for example). It also varies locally within the patch, as implied by the data in figure 14 (discussed later). On the other hand, the temporal evolution of Γ_ρ (from data in figure 7) shows that its value is quite stable during the quasi-steady period, staying around the globally averaged value $\Gamma_\rho \sim 0.13$. This is smaller than 0.2 found in some oceanic applications, but Smyth *et al.* (2001) have shown that the scalar mixing efficiency may vary significantly for different flow cases and parameters. Pham *et al.* (2009) found that in their stably stratified shear layer, $\Gamma = \Gamma_\rho = 0.44$. Pham & Sarkar (2010) suggest, however, that $\Gamma \sim 0.2$ in the turbulent shear layer, whereas for the stably stratified (near) jet turbulence, it exhibits substantial fluctuations and is much larger than 0.2 during the temporal evolution, before becoming closer to 0.2 as the turbulence develops and the dissipation rate increases. Other data give $\Gamma_\rho \sim 0.6$ in the shear layer (Pham & Sarkar 2010) and in turbulent patches formed by the breakdown of K-H billows (Smyth *et al.* 2001), whereas $\Gamma_\rho \sim 0.4$ in turbulent patches in the stably stratified (near) jet (Pham & Sarkar 2010). We may conclude that in our case, since the stagnation zone is inside the wave-breaking patch, the rather smaller values $\Gamma \sim 0.2$ and $\Gamma_\rho \sim 0.13$ may be related to the smaller shear of both velocity and density inside the patch (than, for example, in the shear layer and jet cases).

An alternative definition of the mixing efficiency, introduced by Dornbrack (1998), is the ratio $\mu = \Delta E_p/\Delta E_k$ of the increase $\Delta E_p = E_p(t) - E_p(0)$ in 'turbulent mixing' potential energy to the loss $\Delta E_k = E_k(t) - E_k(0)$ of full kinetic energy $E_k = K_m + k = \langle u_j u_j \rangle/2$ during the mixing event, i.e. the amount of mean-flow kinetic energy $K_m = \langle u_j \rangle \langle u_j \rangle/2$ that has been spent to modify the basic-state stratification irreversibly. The much smaller resulting value of mixing efficiency, $0 \leqslant \mu \leqslant 0.04$, during temporal evolution in the simulations of Dornbrack (1998), in comparison with the above-mentioned levels using conventional scalar-efficiency definitions, is probably connected with use of the specific form of potential energy increase, ΔE_p, which is significantly different from that applied in other studies. The ratio of irreversible potential energy increase (B_i, say) to energy loss by friction has also been used (e.g. Smyth *et al.* 2001), but the evaluation of B_i is far from straightforward for the present flow. We can conclude, nonetheless, that our flow has an overall mixing efficiency (Γ) very similar to those of other general mixing events in stratified flow.

4.3.2. *Dynamics within the turbulent patch*

A more detailed picture of the nature of the TKE processes within the patch, averaged over the quasi-steady period, is provided in figure 14, which shows individual terms over the entire patch area. It is instructive to consider the contribution from each term, with reference to the view of the flow provided by figure 5(d). The rectangular box encapsulating the patch, shown in the latter figure, is re-scaled and included as figure 14(j) to aid the discussion. Notice firstly that the major contribution to shear production is around the lower high-shear region of the patch; there is relatively little

https://doi.org/10.1017/jfm.2011.64 Published online by Cambridge University Press

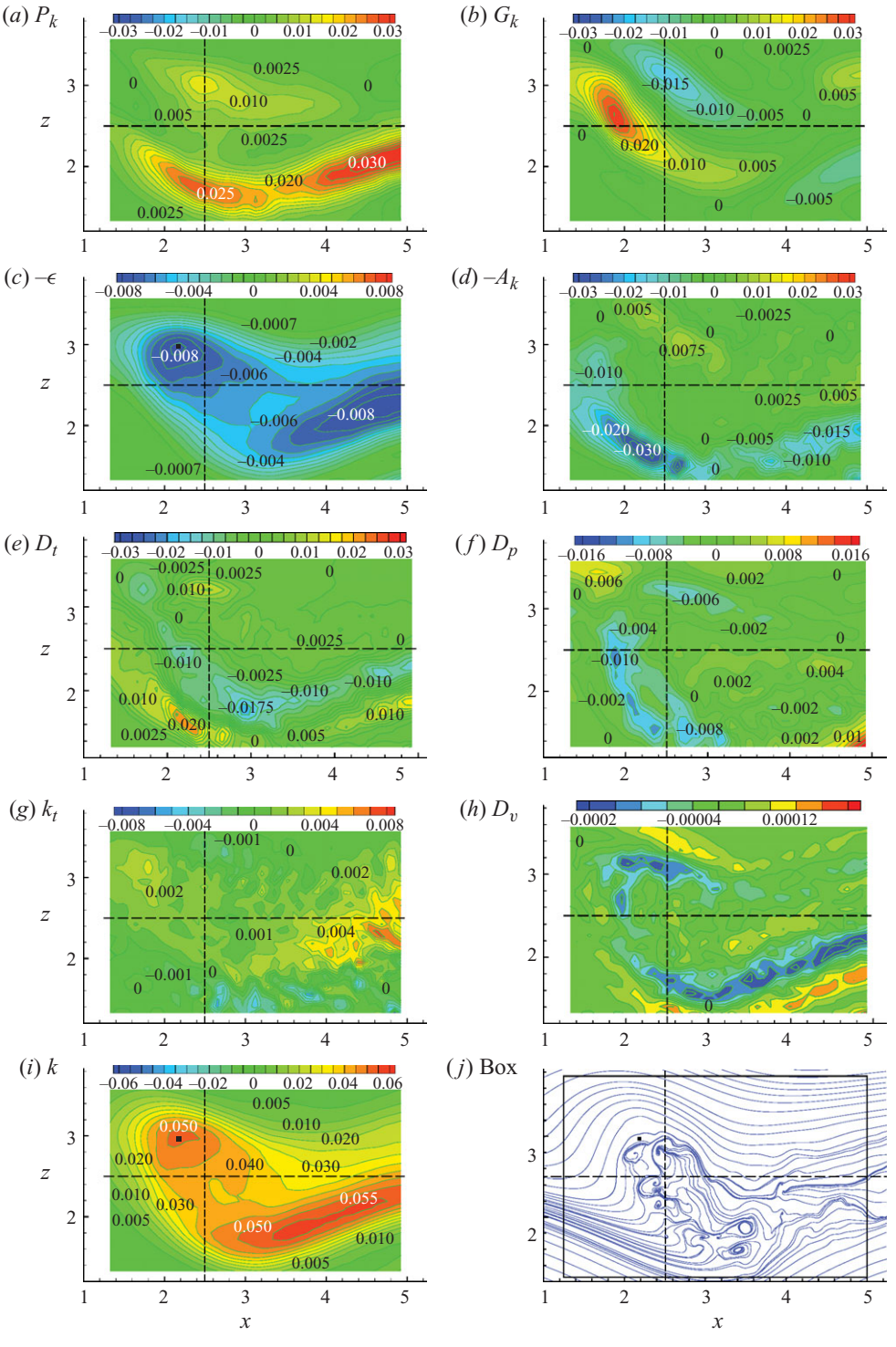


FIGURE 14. TKE balance within the turbulent patch, averaged over the span and over the quasi-steady period ($35 \leqslant t \leqslant 55$). The colour scales differ for many figures, but always red indicates a source, and blue a sink of TKE. Plot (g) shows contours of TKE. Plot (j) gives the instantaneous pathlines shown in figure 5(d), but within a box scaled to be the same as for (a–i). The small black squares in (c, i, j) show the k and ϵ peak area used to compute the temporal spectra in figure 15. Note the relatively very small values in the contour scale for (h).

https://doi.org/10.1017/jfm.2011.64 Published online by Cambridge University Press

in the upper shear-layer region except for a small region around the upstream part, which corresponds to the upper peak in the P_k profile in figure 12(a). An analysis of the various individual contributions to P_k in the patch region (not shown here) shows that the major reason for this is, at its simplest, that the relevant mean velocity gradients, principally $\partial\langle u\rangle/\partial z$, in the lower shear layer are much larger than those in the upper shear layer, by more than a factor of two in the maximum values. TKE production via the two normal stresses (i.e. $-\langle u'u'\rangle\partial\langle u\rangle/\partial z - \langle w'w'\rangle\partial\langle w\rangle/\partial z$) also enhances the total production in the lower frontal region, although the two terms cancel each other around the lower rear of the patch. It is clear that overall the mean shear production, averaged over the whole patch, is positive, as confirmed by the data in figure 13.

Secondly, and in contrast, buoyancy production (figure 14b) occurs solely in the frontal region of the patch and there is some buoyant destruction near the top, as discussed above; this is insufficient to prevent a resultant small positive global average in G_k (see figure 13 and table 1). Note that the positive peak of $G_k = 0.03$ located around $x \sim 1.9, z \sim 2.6$, is entirely responsible for the maximum value of the total production $P_k + G_k = 0.032$ (which is at the same place) since mean shear production is insignificant there. An analysis of the terms contributing to the transport equation for the vertical turbulent flux $\langle\hat{\rho}'w'\rangle$ is instructive. It turns out that the total production of the vertical turbulent flux has the largest peak at the upstream edge of the turbulent patch and is entirely attributable to the behaviour of buoyant production of the buoyancy flux, $-F_h^{-2}\langle\hat{\rho}'\hat{\rho}'\rangle$, and thus to behaviour of the scalar variance, which has a peak in the same area. Furthermore, an analysis of the transport equation for the scalar variance $\langle\hat{\rho}'\hat{\rho}'\rangle$ showed that in the frontal region, the dominant term is $\langle\hat{\rho}'u'\rangle\partial\langle\hat{\rho}\rangle/\partial x$, not because the $\langle\hat{\rho}'u'\rangle$ flux is large (it is actually much less than $\langle\hat{\rho}'w'\rangle$) but because the axial density gradient is quite significant in comparison with the (vanishing) vertical density gradient at the upstream edge of the patch. This fact is clear from figure 5(f), which shows spanwise-averaged pathlines at $t = 40$; because the density contours follow the characteristic S-shaped pathlines, the axial gradients around $x = 2, z = 2.5$ are very large compared with gradients (in either direction) elsewhere. It is this large-scale feature of the flow which eventually leads to strong buoyancy production at the upstream edge of the patch.

Thirdly, significant dissipation (figure 14c) occurs within most of the patch as expected, but particularly where total production (i.e. the 'sum' of the red regions in figures 14a and 14b) is significant. Fourthly, advection of TKE by the mean flow (figure 14d) provides a significant sink of TKE near the lower frontal region of the patch, where the turbulence is being produced by mean shear, suggesting that here the mean flow is advecting the generated turbulence both into the central region of the patch, where it is dissipated, and into regions further downstream and above, where advection terms are positive. Note also that the advection has peak values on a ring around the wave-breaking region. This is because mean velocities are small around the patch centre but increase towards the peripheries and gradients of TKE are also significant at the peripheries.

Fifthly, the turbulence transport term (by triple-velocity products) is generally weak everywhere (in comparison with P_k and A_k for example), as seen in figure 14(e), with source and sink regions providing the low global averages shown in figure 13 and table 1. However, most of the activity, as for shear production, occurs in the lower shear-layer region forming the patch boundary (where TKE gradients are strongest), particularly in its upstream portions. Sixthly, reiterating the comments made earlier, figure 14(f) clarifies that the pressure transport is only really significant (and negative)

https://doi.org/10.1017/jfm.2011.64 Published online by Cambridge University Press

around the outside edges of the regions of dominant shear production (figure 14*a*), suggesting that small-scale wave motions are effective in removing TKE as they propagate. It is the pressure transport which moves the TKE peak slightly away from the place of total production maximum towards that of dissipation. Next, although viscous diffusion (D_v, (4.8)) is included with turbulent transport in figure 14(*e*), figure 14(*h*) confirms that it has levels everywhere below 1 % of the typical maximum level of, say, A_k (figure 14*d*). Finally, the time rate of change of TKE (figure 14*g*), resulting from all these processes, shows no extensive and coherent regions of any significant size. Very small regions of positive and negative values occur with roughly equal probability, so that the global $k_t \approx \partial k/\partial t$ is close to zero (figure 13 and table 1) over most of the patch. Only in the 'tail' of the patch beyond $x = 4$ and around $z = 2.3$ is there any hint of unsteady behaviour, with turbulence levels apparently rising somewhat there. Figure 14(*i*) shows the turbulent kinetic energy field, emphasising the lack of spatial homogeneity (in the x–z plane) within the patch and the relatively large values occurring in regions where the production and dissipation terms are largest.

The clearest features of the TKE balance – i.e. the dominant source of mean-shear production is roughly balanced by the two main sinks of dissipation and advection, whereas buoyancy production and turbulent transport have smaller contributions – are similar to those found on the basis of RANS studies by Richard *et al.* (1989). However, the buoyancy production in their studies was negative in contrast to the global $G_k > 0$ (figure 13 and table 1) in the present work.

4.4. *Deductions from spectral data*

The fact that (shear) production is closely balanced by the sum of dissipation and advection over the whole turbulent patch (so that the rate of change of total turbulent kinetic energy is roughly zero) provides an explanation for why the patch is in an approximately steady state. Only external processes such as the long-time-scale linear mechanism discussed earlier and explained by Rottman *et al.* (1996), which operates on the large-scale low-wavenumber modes, can effect the global motion of the patch. There is no significant region of energy production which is not counterbalanced by dissipation and/or advection, so in a global sense there is no mechanism for rapid growth or decay of the patch. This will only happen on much longer time scales than those typical of the turbulence within the patch.

Temporal turbulent kinetic energy and density fluctuation spectra provide further evidence that buoyancy effects within the patch are very weak. Typical examples are shown in figure 15. These were computed from data collected around $x = 2.19$, $z = 2.97$, the region identified by the small black boxes in figure 14(*c*, *i*, *j*), where the kinetic energy and the dissipation are largest, during the quasi-steady period ($35 \leqslant t \leqslant 55$). Spanwise averaging over 64 nodes was used, i.e. every eighth or fourth node for the finer or coarser grids, respectively; this was sufficient to reduce the scatter to acceptable levels. The results are very similar to those obtained at many other locations within the turbulent patch. As in the spatial spectra discussed earlier (figure 8), there are very clear inertial subranges with a slope of $-5/3$, extending over at least a decade even with the use of the coarser grid ($2560 \times 256 \times 256$). This result is in distinct contrast to that obtained by Gheusi *et al.* (2000), whose spatial spectra within the patch (they do not show temporal spectra) had much larger slopes – typically -2.4 to -3.5 depending on grid resolution – where one would expect the usual inertial subrange. This is almost certainly because of the significantly lower Reynolds number (by more than an order of magnitude) in their computations. Their

https://doi.org/10.1017/jfm.2011.64 Published online by Cambridge University Press

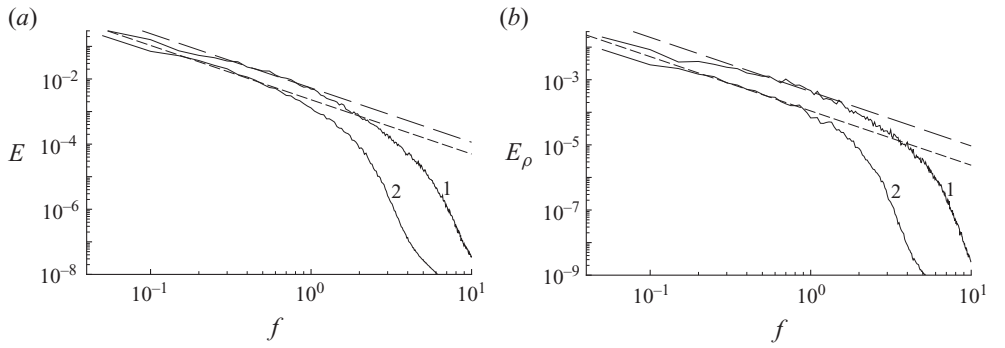


FIGURE 15. (*a*) Turbulent kinetic energy and (*b*) density spectra with two grid resolutions at $x = 2.19, z = 2.97$, averaging along the span. Spectral line numbers: 1, $5120 \times 512 \times 512$; 2, $2560 \times 256 \times 256$; dashed lines have a slope of $-5/3$.

suggestion that viscous dissipation caused this more rapid decay is entirely reasonable. Note that both the spatial spanwise spectrum obtained by Eiff *et al.* (2005) in their higher-Reynolds-number experiments and the LES of Dornbrack (1998), *did* indicate a $-5/3$ region, indicating fully turbulent flow and confirming the results shown in figures 8 and 15.

It has been found in some atmospheric situations that at the lowest wavenumbers (i.e. lower than those within the $-5/3$ inertial subrange), a spectral region of much higher slope can occur. Nastrom & Gage (1985) and Lilly & Kennedy (1973), for example, showed field data which have spectra containing both a f^{-3} and, at higher wavenumber, the usual $f^{-5/3}$ region. The former occurs in the very-long-wavelength part of the spectrum, typically above 1000 km, and is often taken to be symptomatic of an enstrophy cascade in quasi-geostrophic turbulence, associated with large-scale gravity waves. Such scales (even if the present obstacle were assumed to model a 10 km hill) are well beyond the range of the present simulations, so no low-wavenumber region of a slope higher than $-5/3$, arising from wave motions, is expected. Nevertheless, if there were significant buoyancy effects in the patch, there could still be higher slopes at low wavenumbers; Lumley (1964) showed that inertial turbulence in stably stratified flow has a slope of -3 in that range, before reverting to the usual $-5/3$ at higher wavenumber. However, the density profiles typified by figure 10(*b*) show that the patch is fully mixed, so in the present case slopes higher than the usual $-5/3$ are not to be expected until the genuine dissipation range is reached.

It is interesting that the density spectra (figure 15*b*) do not exhibit a significantly less extended range of $-5/3$ slope than seen in the velocity spectra (figure 15*a*). Sreenivasan (1996) has shown that in shear flows, a very high Taylor-microscale Reynolds number, Re_λ, is required before the $-5/3$ scalar spectrum is observed (typically 10^3–10^4). In isotropic turbulence, however, the reverse is true; Warhaft (2000) suggests that for a flow without significant mean strain, 'the mere existence of a multiplicity of scales is apparently enough to produce the $-5/3$ scalar spectrum'. In the present case, Re_λ is larger than 100 (see below), which is usually reckoned to be high enough to see at least some $-5/3$ range in the velocity spectrum, but not (according to Sreenivasan 1996) in the scalar spectrum if there were significant mean shear. So, we conclude that in the present case, the (average) velocity shear in the

https://doi.org/10.1017/jfm.2011.64 Published online by Cambridge University Press

region where the spectra were computed is sufficiently weak not to affect the details of the scalar field.

For spectra containing a clear $-5/3$ region, the inertial subrange data can be used to estimate the dissipation, ϵ, as an alternative to the use of (4.5). With $E(f), \epsilon$ and f normalised using h and U, the subrange relation $E(k_c) = C\epsilon^{2/3}k_c^{-5/3}$ (where k_c is the wavenumber, $2\pi f/u_c$, in the direction of the local convective velocity, $u_c = (\langle u\rangle^2 + \langle v\rangle^2 + \langle w\rangle^2)^{1/2}$) can be written as

$$E(f) = C(2\pi/u_c)^{-2/3}\epsilon^{2/3} f^{-5/3}, \tag{4.11}$$

where C is the Kolmogorov constant for the one-dimensional TKE spectrum. Taking $C = 0.97 = (11/6)C_1$, assuming isotropy and where C_1 is the longitudinal velocity spectrum constant of about 0.53 (Sreenivasan 1995, for example), the data in figure 15(a) suggest $\epsilon = 0.0113$. The value computed directly (from 4.5) at $x = 2.19, z = 2.97$ and shown in figure 14(c) is closer to 0.0085, but this level of agreement might be considered satisfactory, given the usual uncertainties arising from estimating ϵ from the inertial subrange. On the other hand, one should not really expect (4.11) to yield a good estimate for ϵ because in the present flow, Taylor's hypothesis, which is implicitly used in obtaining (4.11) from the spectral relations and assumes low turbulence intensity, is certainly not valid. Over much of the patch, $\sqrt{k}/u_c = O(1)$. Coarser grids naturally yield lower values when computed using (4.5), because the dissipation range is not so accurately resolved, as the spectra shown in figure 15 and computed with a $2560 \times 256 \times 256$ grid indicate. It is therefore possible that even the fine-grid result may be an underestimate, but given that the minimum Kolmogorov scale η, estimated from the (peak) $\epsilon = 0.0085$ value ($\eta = Re^{-3/4}\epsilon^{-1/4}$), is only 0.0065, i.e. $\Delta x = 3.0\eta$, it is unlikely that the error is very large. Mesh sizes of around 5η are usually reckoned to provide adequate resolution (Kim, Moin & Moser 1987; Barri *et al.* 2010). One can also estimate the minimum value of the Kolmogorov time scale, $\tau = (Re\epsilon)^{-1/2} = 0.17$ using the $\epsilon = 0.0085$ value. Since $T_t(= k/\epsilon) \sim 7$ is the largest turbulent scale and the Kolmogorov scale is the smallest, all (non-dimensional) turbulent scales are actually within the range $0.17 < T < 7$. This corresponds roughly to the frequency range $0.05 < f < 2$ shown in figure 15 for the fine-grid runs, confirming that all turbulent time scales are indeed resolved. Defining the length scale $L_t = k^{3/2}/\epsilon$ and with the usual relation for the Taylor microscale, $\lambda = \sqrt{20}\eta^{2/3}L_t^{1/3}$ (Pope 2000), the data yield $Re_\lambda = \sqrt{k}\lambda Re = 157$ at $x = 2.19, z = 2.97$, which is high enough for an inertial subrange to appear in the spectrum, as noted above.

5. Concluding remarks

The nature of a fully developed, two-dimensional turbulent patch arising from the breaking of an internal gravity (lee) wave generated by the presence of bottom topography in a constant velocity and density gradient upstream flow has been explored. Direct numerical simulation at a Reynolds number (based on patch height and upstream velocity) of about 6000 – much higher than previously achieved – has shown that the patch is quasi-steady over a significant time period and has turbulent stress characteristics not dissimilar to those of a classical plane wake. The patch is fully mixed and so both the velocity and density spectra have a substantial $-5/3$ inertial subrange. Buoyancy effects are crucial in the transition period (not explored in this paper) but, once transition is complete, occur largely at the frontal region alone and, averaged over the patch, contribute to a resultant small positive addition to the turbulent kinetic energy. Nonetheless, since this is weak compared to the production

https://doi.org/10.1017/jfm.2011.64 Published online by Cambridge University Press

by shear, there is an approximate global balance between shear production, advection and the dissipation at the smallest scales – explaining why the patch is essentially quasi-steady over a dimensional time period of around $20h/U$, which is at least $O(10)$ buoyancy periods $(1/N)$. It is *not* steady on much longer time scales $(O(100/N))$, because of the persistent generation of upstream-propagating waves, which interact linearly near the obstacle to yield a periodic oscillation of the entire lee-wave system (Rottman *et al.* 1996). Any DNS designed to capture this long-time-scale process as well as resolving details of the turbulent patch would be extremely expensive, even the present computations used over 10^9 grid points.

It should be emphasised that the turbulent patch discussed in this paper is different, at least in its manner of initiation, from that occurring as a result of overturning K-H billows on density and shear interfaces between two regions of (different density) fluid. These have been examined quite extensively (see, for example, Smyth *et al.* 2001) and are characterised throughout their evolution by buoyancy effects, eventually breaking down through the development of stratified layers with associated propagation of gravity waves. Exploration of the rotor arising from separation in the lee of the hill in the present case might reveal some of these features, particularly in the shear layer at its upper edge where K-H billows were noticeable in the computations. The rotor's presence certainly affects the lee-wave region above and, for this case of a 'tuned' obstacle length chosen to maximise the lee-wave amplitudes and trigger wave-breaking, led to the appearance of at least one further elevated turbulent patch some way downstream of the first, as sometimes seen in experiments (Castro *et al.* 1983; Eiff & Bonneton 2000). Although the dynamics of the upper boundary of this lee rotor are different from those leading to breakdown of the elevated patch discussed in this paper, it could well be that, nonetheless, the turbulence characteristics of the rotor (and indeed the secondary elevated wave-breaking region) are not dissimilar to those described here for the primary elevated turbulent patch. Whilst this issue was not the focus of the present work, and would probably require finer meshes in the near-wall region, it could be a fruitful avenue of further work.

Finally, it should be mentioned that in oceanographic (and laboratory towing tank) situations, the Schmidt number is typically 700 if the density variations arise solely through salt concentration. A number of the computations described here were repeated with $Sc = 700$. This of course places severe constraints on the mesh that *ought* to be used, since density gradients within the shear layers surrounding the patch are very much sharper than the velocity gradients and, more importantly perhaps, the scalar dissipation microscale is sufficiently small to imply inadequate resolution of the dissipation range. The resulting density spectra confirmed this, although it seemed that the velocity spectra were only marginally affected. It would be a great challenge to resolve all details of the flow at Schmidt numbers of orders of magnitude larger than unity (as in the oceans). However, the computations suggested that on the large scale of the patch itself, the turbulence characteristics were not greatly different from those presented here. Proper study (via DNS) for such large Schmidt number would require significantly finer grids, however.

The work was supported by DSTL and EPSRC (grant number EP/C008561/1), and made use of the Iridis2 computing resources at the University of Southampton and the HECToR and HPCx facilities at the UK's national high-performance computing services, provided by EPCC at the University of Edinburgh and by the STFC Daresbury Laboratory. The help of staff at the latter is gratefully acknowledged, as is the UK Turbulence Consortium (EPSRC grant number EP/D044073/1), who

https://doi.org/10.1017/jfm.2011.64 Published online by Cambridge University Press

kindly supplemented the available computer resources. We also thank the referees, who made a number of useful suggestions for enhancing the paper.

REFERENCES

Afanasyev, Y. D. & Peltier, W. R. 1998 The three-dimensionalisation of stratified flow over two-dimensional topography. *J. Atmos. Sci.* **55**, 19–39.

Baines, P. G. 1995 *Topographic Effects in Stratified Flows*. CUP.

Barri, M., Khoury, G. K. El, Andersson, H. I. & Petterson, B. 2010 DNS of backward-facing step flow with fully turbulent inflow. *Intl J. Numer. Meth. Fluids* **64**, 777–792.

Bodony, D. J. 2006 Analysis of sponge zones for computational fluid mechanics. *J. Comput. Phys.* **212**, 681–702.

Castro, I. P. & Snyder, W. H. 1993 Experiments on wave breaking in stratified flow over obstacles. *J. Fluid Mech.* **255**, 195–211.

Castro, I. P., Snyder, W. H. & Baines, P. G. 1990 Obstacle drag in stratified flow. *Proc. R. Soc. Lond.* A **429**, 119–140.

Castro, I. P., Snyder, W. H. & Marsh, G. L. 1983 Stratified flow over three-dimensional ridges. *J. Fluid Mech.* **135**, 261–282.

Clark, T. L., Hall, W. D., Kerr, R. M. & Middleton, D. 2000 Origins of aircraft-damaging clear-air turbulence during the 9 December 1992 Colorado downslope windstorm: numerical simulations and comparison with observations. *J. Atmos. Sci.* **57**, 1105–1131.

Clarke, T. L. & Peltier, W. R. 1977 On the evolution and stability of finite-amplitude mountain waves. *J. Atmos. Sci.* **34**, 1715–1730.

Dornbrack, A. 1998 Turbulent mixing by breaking gravity waves. *J. Fluid Mech.* **375**, 113–141.

Doyle, J. D. & Durran, D. R. 2007 Rotor and subrotor dynamics in the lee of three-dimensional terrain. *J. Atmos. Sci.* **64**, 4202–4221.

Doyle, J. D., Shapiro, M. A., Jiang, Q. & Bartels, D. I. 2005 Large-amplitude mountain wave breaking over Greenland. *J. Atmos. Sci.* **62**, 3106–3126.

Eiff, O. F. & Bonneton, P. 2000 Lee-wave breaking over obstacles in stratified flow. *Phys. Fluids* **12**, 1073–1086.

Eiff, O., Huteau, F. & Tolu, J. 2005 High-Reynolds-number orographic wave-breaking experiments. *Dyn. Atmos. Oceans* **40**, 71–89.

Gheusi, F., Stein, J. & Eiff, O. F. 2000 A numerical study of three-dimensional orographic gravity-wave breaking observed in a hydraulic tank. *J. Fluid Mech.* **410**, 67–99.

Grubisic, V. & Lewis, J. M. 2004 Sierra wave project revisited: 50 years later. *Bull. Am. Meteorol. Soc.* **85**, 1127–1142.

Ivey, G. N. & Imberger, J. 1991 On the nature of turbulence in a stratified fluid. Part I. The energetics of mixing. *J. Phys. Oceanogr.* **21**, 650–658.

Kim, J., Moin, P. & Moser, R. 1987 Turbulence statistics in fully developed turbulent channel flow at low Reynolds number. *J. Fluid Mech.* **177**, 133–166.

Klemp, J. B. & Lilly, D. K. 1977 Numerical simulation of hydrostatic mountain waves. *J. Atmos. Sci.* **35**, 78–107.

Lilley, D. K. & Klemp, J. B. 1979 The effects of terrain shape on nonlinear hydrostatic mountain waves. *J. Fluid Mech.* **95**, 241–261.

Lilly, D. K. & Kennedy, P. J. 1973 Observations of a stationary mountain wave and its associated momentum flux and energy dissipation. *J. Atmos. Sci.* **30**, 1135–1152.

Long, R. R. 1955 Some aspects of flow of stratified fluids. III. continuous density gradients. *Tellus* **7**, 341–357.

Lumley, J. 1964 The spectrum of nearly inertial turbulence in a stably stratified fluid. *J. Atmos. Sci.* **21**, 99–102.

Nastrom, G. D. & Gage, K. S. 1985 A climatology of atmospheric wavenumber spectra of wind and temperature observed by commercial aircraft. *J. Atmos. Sci.* **42**, 950–960.

Paisley, M. F. & Castro, I. P. 1995 Numerical experiments of stratified flow over three-dimensional obstacles. In *Numerical Methods for Fluid Dynamics V* (ed. K. W. Morton & M. J. Baines), pp. 523–531. Oxford University Press.

https://doi.org/10.1017/jfm.2011.64 Published online by Cambridge University Press

Paisley, M. F. & Castro, I. P. 1996 A numerical study of wave-breaking in stratified flow over obstacles. *Dyn. Atmos. Oceans* **23**, 309–319.

Pham, H. T. & Sarkar, S. 2010 Internal waves and turbulence in a stable stratified jet. *J. Fluid Mech.* **648**, 297–324.

Pham, H. T., Sarkar, S. & Brucker, K. A. 2009 Dynamics of a stratified shear layer above a region of uniform stratification. *J. Fluid Mech.* **630**, 191–223.

Pope, S. B. 2000 *Turbulent Flows*. CUP.

Richard, E., Mascart, P. & Nickerson, E. 1989 On the role of surface friction in downslope windstorms. *J. Appl. Meteorol.* **28**, 241–251.

Rottman, J. W., Broutman, D. & Grimshaw, R. 1996 Numerical simulations of uniformly stratified flow over topography. *J. Fluid Mech.* **306**, 1–30.

Scinocca, J. & Peltier, W. R. 1993 The instability of Long's stationary solution and the evolution toward severe downslope windstorm flow. Part I. Nested grid numerical simulation. *J. Atmos. Sci.* **50**, 2245–2263.

Smith, R. B. 1985 On severe downslope winds. *J. Atmos. Sci.* **42,** 2597–2603.

Smyth, W. D., Hebert, D. & Moum, J. N. 1996 Local ocean response to a multiphase westerly wind burst. Part 2. Thermal and fresh water responses. *J. Geophys. Res.* **101** (C10), 22513–22533.

Smyth, W. D., Moum, J. N. & Caldwell, D. R. 2001 The efficiency of mixing in turbulent patches: inferences from direct simulations and microstructure observations. *J. Phys. Oceanogr.* **31**, 1969–1992.

Sreenivasan, K. R. 1995 On the universality of the Kolmogorov constant. *Phys. Fluids* **7**, 2778–2784.

Sreenivasan, K. R. 1996 The passive scalar spectrum and the Obukhov–Corrsin constant. *Phys. Fluids* **8**, 189–196.

Sveen, J. K., Guo, Y., Davies, P. A. & Grue, J. 2002 On the breaking of internal solitary waves at a ridge. *J. Fluid Mech.* **469**, 161–188.

Thomas, T. G. & Williams, J. J. R. 1997 Development of a parallel code to simulate skewed flow over a bluff body. *J. Wind Engng Ind. Aerodyn.* **67–68**, 155–167.

Townsend, A. A. 1976 *The Structure of Turbulent Shear Flow*, 2nd edn. CUP.

Voropayev, S. I., Afanasyev, Y. D. & van Heijst, G. J. F. 1993 Experiments on the evolution of gravitational instability of an overturned, initially stably stratified fluid. *Phys. Fluids* A **5**, 2461–2466.

Warhaft, Z. 2000 Passive scalars in turbulent flows. *Annu. Rev. Fluid Mech.* **32**, 203–240.

Yakovenko, S. N., Thomas, T. G. & Castro, I. P. 2009 DNS of turbulence in breaking waves. Parts I–IV. Internal reports, AFM08.3, 8.4, 9.1 and 9.3. University of Southampton.

Ying, Q. & Baopu, F. 1993 Turbulence in broken lee waves. *Acta Mechanica Sin.* **9**, 210–222.

Zhou, Y. & Antonia, R. A. 1995 Memory effects in a turbulent plane wake. *Exp. Fluids* **19**, 112–120.

https://doi.org/10.1017/jfm.2011.64 Published online by Cambridge University Press